Amorphous 2D-Nanoplatelets of Red Phosphorus Obtained by Liquid-Phase Exfoliation Yield High Areal Capacity Na-Ion Battery Anodes

Harneet Kaur, Bharathi Konkena, Cian Gabbett, Ross Smith, Mark McCrystall, Ruiyuan Tian, Ahin Roy, Tian Carey, Victor Vega-Mayoral, Valeria Nicolosi, and Jonathan N. Coleman

The development of sodium ion batteries will require high-performance electrodes with very large areal capacity and reasonable rate performance. Although red phosphorus is a very promising electrode material, it has not yet fulfilled these requirements. Here, liquid phase exfoliation is used to convert solid red phosphorus into amorphous, quasi-2D nanoplatelets. These nanoplatelets have lateral sizes of hundreds of nanometers, thickness of 10s of nanometers and are quite stable in ambient conditions, displaying only low levels of oxidation on the nanosheet surface. By solution mixing with carbon nanotubes, these nanoplatelets can be fabricated into nanocomposite battery anodes. After employing an extended activation process, good cycling stability over 1000 cycles and low-rate capacitances >2000 mAh g_P^{-1} is achieved. Because of the high conductivity and mechanical robustness provided by the nanotube network, it is possible to fabricate very thick electrodes. These electrodes display extremely high areal capacities approaching 10 mAh cm^{-2} at currents of ≈1 mA cm^{-2}. Detailed analysis shows these electrodes to be limited by solid-state diffusion such that the thickest electrodes have state-of-the-art rate performance and a near-optimized combination of capacity and rate performance.

H. Kaur, B. Konkena, C. Gabbett, R. Smith, M. McCrystall, R. Tian,
T. Carey, J. N. Coleman
School of Physics
CRANN & AMBER Research Centre
Trinity College Dublin
Dublin 2, Ireland
E-mail: colemaj@tcd.ie
A. Roy, V. Nicolosi
School of Chemistry
CRANN & AMBER Research Centre
Trinity College Dublin
Dublin 2, Ireland
V. Vega-Mayoral
Madrid Institute for Advanced Studies
IMDEA Nanociencia
Calle Faraday 9, Madrid 28049, Spain

The ORCID identification number(s) for the author(s) of this article can be found under https://doi.org/10.1002/aenm.202203013.

1. Introduction

Because of the limited global availability of lithium, it is well-known that alternatives to lithium ion batteries are required for near future.[1] The most obvious alternative is the sodium-ion battery (SIB) because of sodium's greater earth abundance and lower cost.[2,3] Developing suitable sodium storing materials for both cathode and anodes is one of the major challenges in SIB research. Successful electrode materials should have appropriate Na storage potentials, high specific capacity, good cycling stability and be suitable for fabrication into reasonably thick electrodes with high areal capacity and energy density coupled with reasonable rate performance.

Phosphorus (P) has been found to be one of the most promising anode materials for SIBs due to its high theoretical capacity (2595 mAh g^{-1}), low-cost, and natural abundance.[4] In terms of SIBs, both black and red phosphorous have received much attention (see Table S1, Supporting Information, for literature review). Black P (BP) is promising because its layered structure should enable Na ion diffusion while its reasonably high electrical conductivity should facilitate charge transport.[5,6] However, black P is expensive to synthesize with no scalable production method available.[7] In addition, achieving high specific capacities (>2000 mAh g_P^{-1}) has required very high additive (binder and conductive additive) loadings of ≥35 wt%, leading to reduced total-electrode-mass-normalized capacities below 1500 mAh g_{total}^{-1} (see Table S1, Supporting Information). Alternatively, red P (RP) has attracted a lot of attention as an SIB anode material owing to its abundance, low cost, and high chemical stability.[8–10] In addition, specific capacities beyond 2000 mAh g_P^{-1} have been achieved at relatively low additive loadings of 20%.[11] However, RP suffers from very slow Na ion solid state diffusivity[12] which limits rate performance as well as large volume expansion (≈300%) during cycling[8–10] which can result in severe electrode pulverization.[13–15] In addition, for both BP and RP, work has focused on thin electrodes with mass loadings of <2 mg cm^{-2} (thickness <20 μm, Table S1, Supporting Information). This has limited the reported areal capacities to values no higher than 1.7 mAh cm^{-2}.[10]

**ADVANCED
SCIENCE NEWS**

www.advancedsciencenews.com

**ADVANCED
ENERGY
MATERIALS**

www.advenergymat.de

Thus, it is clear that while both BP and RP show great promise, much work is required to allow phosphorous to reach its full potential as a Na storing material. This will require developing P-based anodes with near-theoretical specific capacity (mAh g_P^{-1}), while achieving this at low additive-content so that the total-electrode-mass-normalized capacity (mAh g_{total}^{-1}) remains high. Such performance must be accomplished in a form of phosphorous that enables good rate performance, that is where solid state diffusion times are not too high, and yields stable cycling. In addition, it will be necessary to achieve high performance in thick electrodes to maximize the areal capacity (mAh cm^{-2}).

Due to its lower cost, more attention seems to have been paid to RP as compared to BP. As with other electrode materials, two important strategies have been used to maximize the performance of RP-based electrodes, that is, the reduction of the phosphorous particle size in order to reduce solid-state diffusion times, and the optimization of conductive additives to enhance charge delivery and impart mechanical robustness to stabilize electrodes during expansion/contraction.[16,17]

Reducing the size of active particles is an important strategy in the optimization of both Li and Na storing electrodes. Using small active particles has two main advantages. It allows the conductive additive network to effectively deliver charge to all parts of the electrode and leads to short ion diffusive paths, leading to reduced solid-state diffusion times.[18] In RP-based electrodes the active particles are usually quasi-spherical with size in the range nm to μm.[16,17] While using small particles leads to enhanced capacity and improved rate performance,[19–22] their small size (<60 nm) is also problematic as it leads to very large surface areas which results in amplified consumption of sodium during SEI formation and increased parasitic side reactions with the electrolyte.[18,23]

The optimization of conductive additives has ranged from mixing RP particles with graphene,[24] nanotubes,[25] nanofibers,[26] and carbon black,[5] to more complex strategies involving coating RP particles with carbonaceous layers.[16,17] In all cases, the aim is to enhance conductivity in order to deliver charge throughout the electrode while allowing the electrode to accommodate the expansion/contraction associated with sodiation/desodiation.

We propose that a promising approach to optimizing both particle size and conductive additive is to utilize the active material (here RP) in the form of 2D platelets which are then combined with a network of carbon nanotubes which acts as both binder and conductive additive. In terms of geometry, platelets have an advantage over spherical particles because, for a given solid state diffusion length (i.e., thickness, they have × 3 less surface area per volume. This allows us to minimize the solid-state diffusion length (i.e., half the platelet thickness) without incurring the same increase in surface area associated with spherical particles. In addition, for smaller platelets, the nanotube network effectively delivers charge as evidenced by the very high capacities routinely achieved in electrodes prepared from mixtures of nanotubes and 2D-active materials.[27–30] Using a nanotube network as a conductive additive has the advantage that it yields higher conductivity at lower loading than either 2D or 0D fillers.[31] Nanotube networks also impart mechanical robustness in a way that graphene or carbon

black based networks cannot,[32] allowing them to be used as both binder as well as the conductive additive.[27,33] This is evidenced by the superlative performance of super thick electrodes fabricated using carbon nanotubes.[33]

Liquid-phase exfoliation (LPE) is well known process used to produce 2D nano-platelets, usually by the exfoliation of layered compounds.[34–36] For layered compounds, the LPE mechanism consists of two main processes which takes place simultaneously when these materials are subjected to sonic energy in a suitable solvent.[37] The first process is the "exfoliation" in which van der Waals forces between the layers are broken resulting in the decrease in thickness and the other is "fragmentation" consisting of breaking in strong in-plane covalent bonds resulting in a reduction of lateral dimensions.[37] The energy required to break the van der Waals forces is far smaller than what is needed for fragmentation resulting in a 2D morphology of the exfoliated product which are referred as "nanosheets."[38] However, recently we and others have observed that non-layered bulk materials such as Fe_2O_3,[39] FeS_2,[40] FeF3,[41] α-Ge,[42] Si,[43] etc., can also be exfoliated into nanoplatelets by LPE.[39–42,44–46] However, in such a system, the only process taking place is fragmentation, that is, rupturing of bonds by the sonication-induced microjets.[46] It is still unknown why this process results in the formation of 2D platelets rather than quasi-spherical nanoparticles.[46] Such questions are difficult to answer and require more studies in this direction.[46] But clearly, LPE can be used to convert non-layered materials into nanoplatelets.[46]

In this work, we will build on these recent advances[39–45,47–51] on liquid-exfoliation of nonlayered non-van der Waals materials.[46] In the first part of the paper we will use this approach to convert solid red phosphorous into nanoplatelets which we will fully characterize. In the second part of the paper, we will characterize their ability to store sodium by mixing them with carbon nanotubes to form SIB anodes. These anodes display state-of-the-art total-electrode-mass-normalized capacities of ≈1750 mAh g_{total}^{-1} and very good stability. The mechanical robustness imparted by the carbon nanotubes allows us to fabricate thick electrodes up to 170 microns thick which display areal capacities approaching 10 mAh cm^{-2} far above the previous state-of-the-art. Considering their thickness, these electrodes display excellent rate performance with our thickest electrodes displaying and near optimize combination of capacity and rate performance.

2. Results and Discussion

2.1. Liquid Processing of Red P into Nanoplatelets

2.1.1. Production of Nanoplatelets by Liquid-Phase Exfoliation

As shown in the inset of **Figure 1**A, commercial RP consists of red/brown solid pieces of size 0.5–5 mm. RP is known to be amorphous and thought to consist of polymeric chains of phosphorous atoms.[52] These pieces were crushed in the presence of N-methyl-2-pyrollidone (NMP) solvent to reduce their size to ≈0.1–1 mm prior to sonication (details are described in Section 4 and Figure S1, Supporting Information). After probe
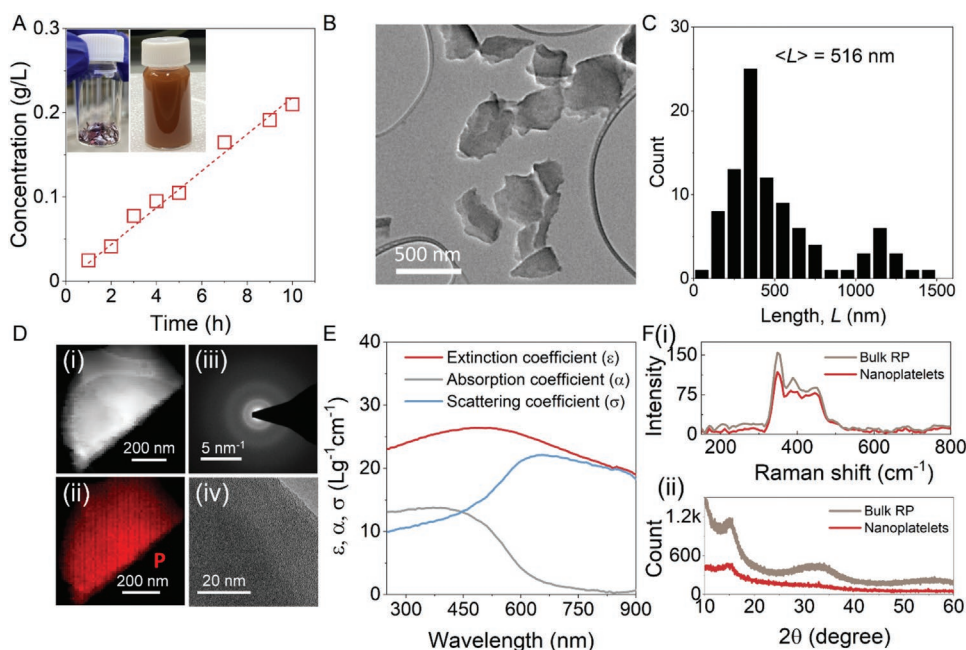
Figure 1. Exfoliation of red phosphorus solids into nanoplatelets. A) Plot of concentration of the dispersion as a function of probe sonication time depicted a linear behaviour (linear fit is shown by the dotted line) where the slope gives the rate of production of nanoplatelets. Inset shows the photo of RP bulk solids and the dispersion obtained after 10 h of LPE process. B) TEM image of the exfoliated nanoplatelets. C) Length, L histogram of the nanoplatelets in std-RP dispersion obtained by TEM image analysis using ImageJ software. Statistical analysis revealed mean length $<L>$ of 516 ± 32 nm. D) HR-TEM image of a i) nanoplatelet, and ii) its corresponding EDAX map, iii) diffraction pattern, and iv) high-resolution image. E) Absorption, extinction, and scattering coefficient spectra of the std-RP dispersion. F) i) Raman spectra and ii) XRD of the bulk solids and nanoplatelets of RP, respectively.

sonication in 80 mL NMP for various times up to 10 h, the as-obtained dispersions were centrifuged at 100 g to remove large particles and unexfoliated material. The resultant supernatant was solvent-exchanged from 80 mL NMP to 80 mL 2-isopropanol by centrifugation at 3660 g and redispersion of the sediment via 10 min of bath sonication. We refer to the dispersion obtained after solvent exchange as the standard sample (std-RP). It exhibits a red/brown color and is shown in the inset of Figure 1A.

The concentration was carefully measured by filtration and weighing for various sonication times (in NMP) as shown in Figure 1A. We find the concentration (C) to scale linearly with the probe sonication time yielding a constant production rate of 0.02 g L^{-1} h. This linear increase is clearly different to the $C \propto (\text{time})^{1/2}$ behavior usually found for LPE of layered crystals.[53,54] As proposed by Texter,[55] the usual square-root dependence is linked to diffusion of solvent into the van der Waals gap of the layered crystal, something that doesn't occur in the exfoliation of non-layered materials. Thus, this change in t-dependence is likely due to mechanistic differences between exfoliation of layered and nonlayered materials. We also note that the yield obtained after 10 h of probe sonication was 1.1 wt% which is very low as compared to the yield produced by LPE of layered vdW compounds which can be as high as 100%.[56] However, these results are in line with the observed yield of 1–4% for the LPE of nonlayered compounds.[46]

The nature of the material produced by the process described above was examined by transmission electron microscopy (TEM). TEM imaging (Figure 1B) showed a large number of

nano-objects which appeared to be quasi-2D in nature, consistent with the production of nanoplatelets. This quasi-2D geometry will be confirmed below. To assess the lateral dimensions of these nanoplatelets, statistical analysis was performed ((Figure 1C) which showed a bimodal length distribution with modes at $L \approx 400$ nm and $L \approx 1100$ nm and an average length of $<L> \approx 516$ nm. High-resolution TEM equipped with energy dispersive X-ray (EDAX) detector was also used to further examine the structure and composition of these objects. Figure 1D-i) shows an image of a nanoplatelet with the corresponding elemental composition map (Figure 1D-ii) showing a uniform distribution of phosphorus atoms throughout the nanoplatelet. Selected area electron diffraction (SAED) pattern captured on the nanoplatelet (Figure 1D-iii) shows the absence of diffraction spots while high-resolution TEM imaging (Figure 1D-iv) shows the absence of lattice fringes, confirming the amorphous nature of the nanoplatelets.

We performed optical characterization of the standard dispersion by measuring the extinction coefficient (ε) spectrum (ε is defined by $T = 10^{-\varepsilon Cl}$, where T is the measured optical transmittance, C is the concentration of the dispersion measured by filtering and weighing, and l is the path length of the cuvette). As shown in Figure 1E, the extinction coefficient spectrum is broad and featureless and, like other nano-red P samples,[57,58] displays relatively strong extinction in the visible region. As with many dispersed 2D materials this is partly due to the presence of light scattering.[59,60] An integrating sphere was used to obtain the contribution of scattering (σ) allowing us to extract the absorbance (α) spectrum via (Figure 1E)

$$\varepsilon(\lambda) = \sigma(\lambda) + \alpha(\lambda) \tag{1}$$

The absorption spectrum shown a band-edge at ≈650 nm confirming the semiconducting nature of these amorphous nanoplatelets. This yields an optical bandgap ≈1.9 eV which is consistent with bandgap of amorphous RP nanoparticles (1.9–2.1 eV).[57,58,61]

We investigated the structure of the RP nanoplatelets using Raman spectroscopy and X-ray diffraction (XRD) performed on thin, drop-cast films. Figure 1F-i shows the Raman spectrum of the exfoliated nanoplatelets compared to the bulk RP material. Both bulk and exfoliated material show the same Raman spectral features indicating that the bonding scheme remains preserved after liquid exfoliation. No additional Raman modes were observed. Note that we have not assigned these Raman modes as assignment depends upon the structural model proposed for the amorphous red phosphorus which is still under discussion.[58,62] Figure 1F-ii shows the XRD spectra of the bulk and exfoliated RP. Both bulk and phosphorous nanoplatelets show the presence of the characteristic broad diffraction peaks which is ascribed to the medium range ordered structure of phosphorus atoms in amorphous red phosphorus.[63,64] No other diffraction peak was observed implying high purity of the nanoplatelets, and no diffraction peaks corresponding to the bulk oxidation were found. These results are consistent with the Raman spectroscopy results.

2.1.2. Aspect Ratio of Nanoplatelets

While nanosheets prepared by liquid phase exfoliation of layered materials are expected to have high aspect ratio (length/thickness),[38] nanoplatelets produced by LPE of non-layered materials are not.[46] This makes it very important to carefully measure the dimensions of nano-objects produced by LPE of non-layered materials in order to determine their geometry and assess their dimensionality via their aspect ratio.[46] Here, we used liquid cascade centrifugation[65] to size-select the exfoliated material into fractions with different size ranges. We then used statistical atomic force microscopy (AFM) analysis[40,41] to measure the dimensions of 80–100 platelets in each fraction. **Figure 2**A shows examples of AFM images obtained for the largest (g-force range 100–400 g) and the smallest fraction (g-force range 2000–3660 g). The length (L) and thickness (t) histograms of these fractions are displayed in Figure 2B. The complete set of histograms with AFM images of all the fractions (Figure S2, Supporting Information) and histograms obtained from the TEM images of the largest and the smallest fraction (Figure S3, Supporting Information) are given in Supporting Information.

From AFM data such as those shown in Figure 2A,B, we calculated average values of the nanoplatelets length, $\langle L \rangle$, width, $\langle W \rangle$, and thickness, $\langle t \rangle$ for each fraction. These are plotted versus the central centrifugal acceleration (expressed in terms of g) used during liquid cascade centrifuge as shown in Figure 2C. We found that the dimensions of the nanoplatelets scales roughly as (g-force)$^{-1/2}$ similar to what has been observed for the nanosheets produced by liquid exfoliation of various 2D materials.[38,54]

The data in Figure 2C shows that the objects produced by LPE of RP have lengths considerably larger than their thickness confirming them to be quasi-2D in geometry. We note that the lateral size of these nanoplatelets is in the same range as nanosheets produced by LPE of layered compounds (≈50–700 nm).[38] However, the thickness of these nanoplatelets is typically tens of nanometers, considerably higher than values of <10 nm usually observed for nanosheets produced from layered materials.[38] This is to be expected given the greater energies required to exfoliate non-layered materials.[46]

To understand the nanoplatelet dimensions in more detail, we plot the nanoplatelet area (defined as $A = LW$) versus thickness, t, on a platelet-by-platelet basis as shown in Figure 2D. This is of interest because a recent model on the mechanisms of LPE has predicted that nanosheet area should scale with thickness as a power law, behavior that is observed in experiments for many layered materials.[37,38] We do find power-law behavior with an exponent of 1.67 ($A \propto t^{1.67}$) as shown in Figure 2D. However, it is worth noting that for nanosheets produced by LPE of layered materials,[38] this exponent tends to be >2, suggesting LPE of non-layered material might have some mechanistic differences.

To investigate the quasi-2D nature of these nanosheets in more detail we have calculated two different aspect ratios, $k_1 = L/t$, and $k_2 = L/W$ for each individual nanoplatelet. We plotted both L/t and L/W versus t on a platelet-by-platelet basis in Figure 2E,F to test the dimensionality of the nanoplatelets. As shown in the Figure 2E, the aspect ratio L/t appears to scale weakly with t such that very thin nanoplatelets have high L/t-aspect ratios (maximum value 18) while the thicker nanoplatelets have much lower L/t-aspect ratios (minimum value of 3). We note that such an increase in aspect ratio as nanoplatelet thickness is reduced has been observed before for other liquid-exfoliated non-layered compounds, FeF$_3$ and FeS$_2$.[40,41] As such, this behavior may be a feature of LPE of non-layered materials. Overall, the mean aspect ratio of the nanoplatelets is 7. Note that this value is quite low is of course linked to the fact that these nanosheets are quite thick which is in turn linked to the fact that there is no easily cleavage plane in amorphous RP.[46] Shown in Figure 2F, is the length/width aspect ratio, L/W, plotted versus t on a platelet-by-platelet basis. We find L/W to be independent of thickness and vary between ≈1 and 4 with a mean of 2.2.

We note that the data above clearly demonstrates that liquid phase exfoliation can be used to produce quasi 2D platelets of red phosphorus. Although a number of non-layered materials have been exfoliated using LPE,[46] we believe this is the first time an amorphous material has been converted into 2D nanoplatelets in this way.

2.1.3. Stability in Ambient

From an application viewpoint, it is crucial to examine the temporal stability of the RP nanoplatelets. To test this, we measured absorbance spectra of the std-RP dispersion in IPA at various times from 0 to 216 h after exfoliation. To avoid the effects of sedimentation, the dispersion was bath sonicated for 2 min prior to each measurement. As shown in **Figure 3**A,

**ADVANCED
SCIENCE NEWS**

www.advancedsciencenews.com
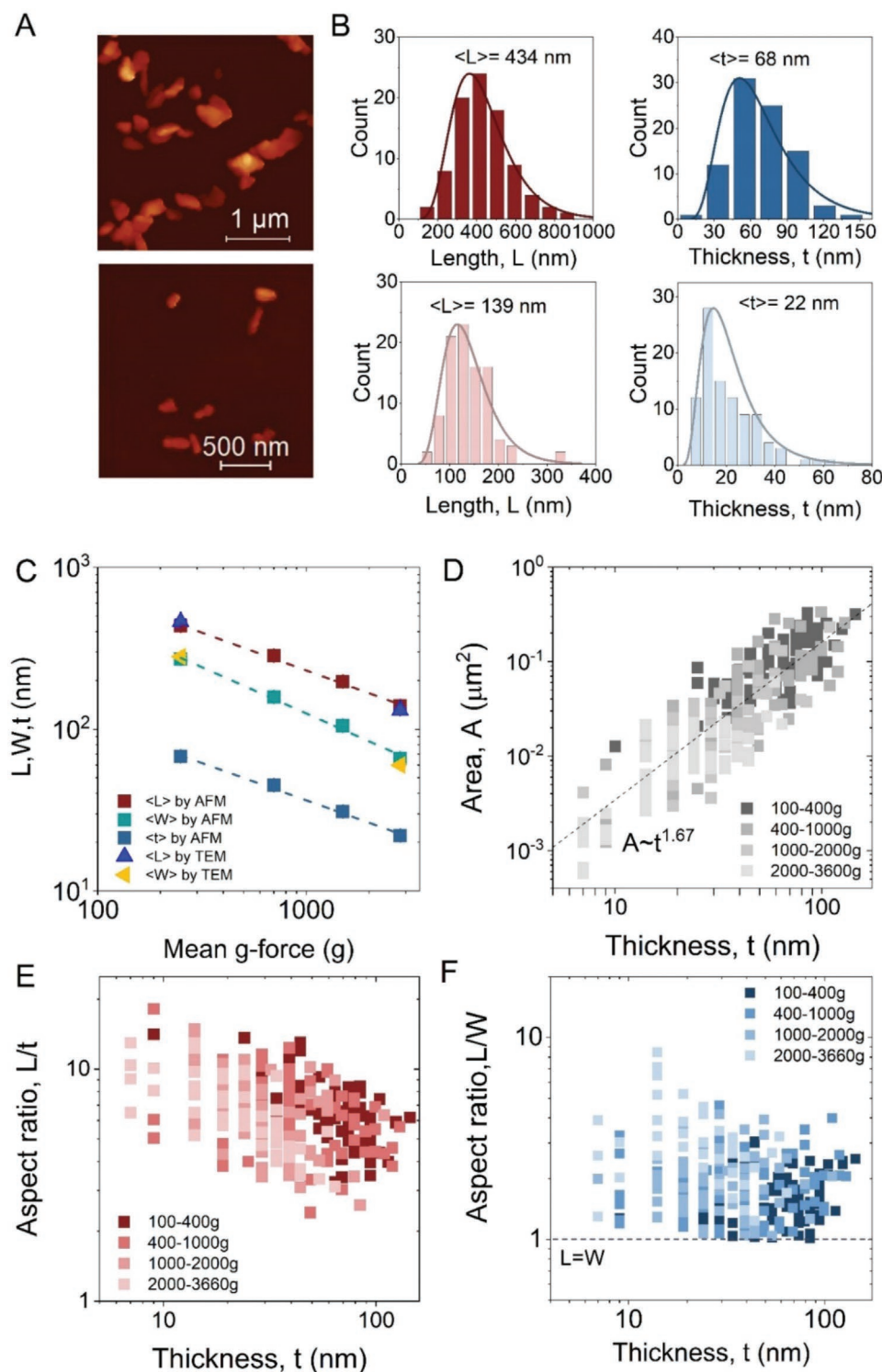
**ADVANCED
ENERGY
MATERIALS**

www.advenergymat.de

Figure 2. Length, width and thickness analysis of red-P nanoplatelets by AFM and TEM. A) AFM image of the largest (top) and smallest fraction (bottom) of the nanoplatelets obtained by using liquid-cascade centrifuge (LCC). B) Distribution plots of the length, L and thickness, t of the largest (top), and the smallest fraction (bottom) of nanoplatelets. C) Variation in the mean $<L>$, $<W>$, and $<t>$ of the nanoplatelets as a function of mean centrifugal force (g-force) used during LCC. D) Area ($A = LW$) of nanoplatelets versus t plot. The dashed line represents a fit to the data points. E,F) Aspect ratio L/t versus t plot, and L/W versus t plot. Each point on the graph represents an individual nanoplatelet. A total of 360 nanoplatelets were counted, 90 from each fraction of different sizes.
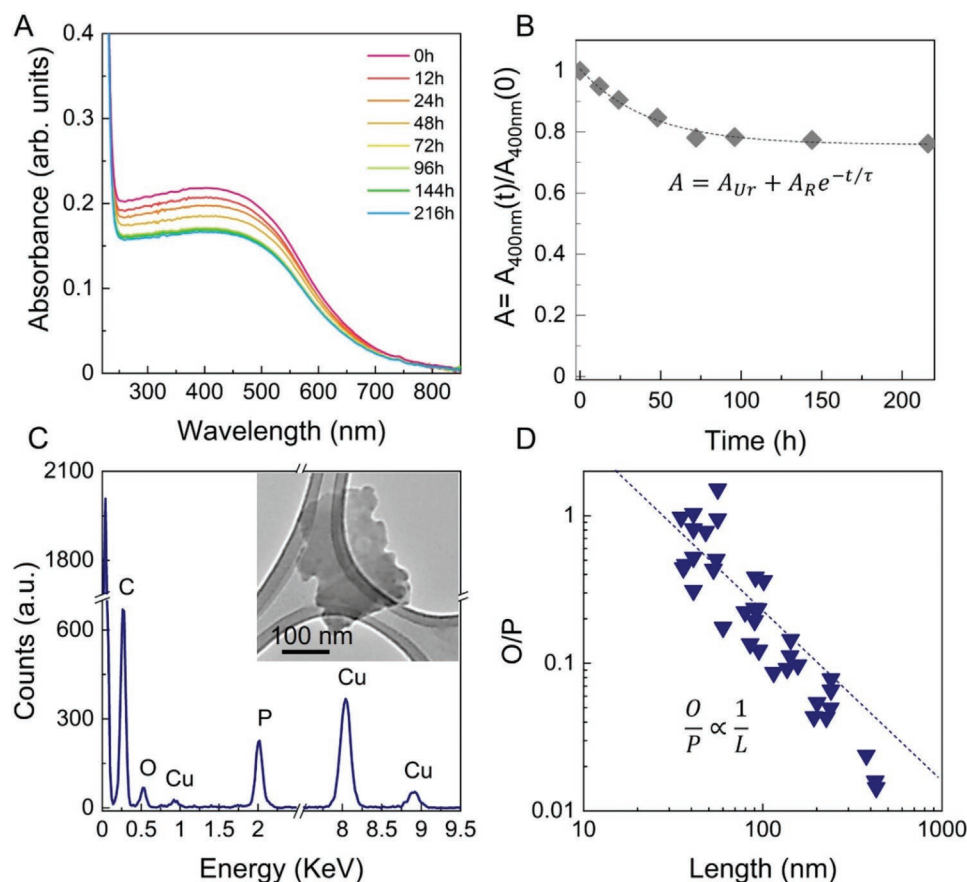
Figure 3. Stability studies of red phosphorus nanoplatelets. A) Absorbance of std-RP dispersion versus wavelength as a function of time. B) Shows the data points of the relative absorbance, A at 400 nm with time. Dashed line represents a fit with exponential decay equation: $A = A_{Ur} + A_R e^{-t/\tau}$ where A_{Ur} represent the unreacted component and A_R represents the total amount of nanoplatelets which reacts over time. C) EDAX spectra acquired on an individual platelet as shown in the inset showed the presence of C, O, Cu, and P elements. The C and Cu signal is from the TEM grid. D) Atomic ratio of the oxygen to phosphorus elements in individual nanoplatelets versus the length of the nanoplatelets. Each data point represents an individual nanoplatelet. A total of 35 nanoplatelets were individually measured. The dashed line represents an inverse relationship between the atomic ratio (O/P) with length (L) and the data is fitted by Equation (1).

the measured absorbance showed no observable changes in spectral shape with time, indicating that the measured absorbance is dominated by as-produced RP.

However, the absorbance falls over time, perhaps due to the oxidation of some P atoms. To quantify this, we plotted the normalized absorbance at $\lambda = 400$ nm (A) as a function of time in Figure 3B. The data points were fit to an empirical equation of the form:

$$A = A_{Ur} + A_R e^{-t/\tau} \quad (2)$$

where A_{Ur} represent the unreacted component and A_R represents the total amount of nanoplatelets which reacts over time.[66] The fit to the equation yields: $A_{Ur} = 0.76$, $A_R = 0.24$, and $\tau = 42.3 \pm 5.8$ h. This implies a degradation timescale of roughly 2 days and that 24% of P atoms will eventually oxidize in the dispersion. This suggests that the RP nanoplatelets are more stable than black phosphorus nanosheets for which 50% of P atoms degraded in IPA solvent after long times.[66] We further studied the ambient stability of RP nanoplatelets in solid-phase by tracking extinction spectroscopy and SEM/EDAX elemental

maps of filtered films over a time period of 8 days as shown in Figure S4, Supporting Information. The analysis of the data confirms the surface oxidation of nanoplatelets during exfoliation and a high stability of deposited nanoplatelets in ambient conditions, with very little change in either optical properties or oxygen content after 8 days of air exposure.

To study the nature of the degradation in the liquid phase, the surface chemistry of the nanoplatelets was studied with FT-IR spectra (Figure S5, Supporting Information) which showed clear stretching peaks of P—O, P = O, and P—OH at 1080, 1190, 1653 cm^{-1}, respectively and a broad peak (O—H stretching) at 3300 cm^{-1}.[64,67] This confirms the hypothesis above that RP nanoplatelets suffers some oxidation during exfoliation. As shown in the Figure 3C, EDAX spectroscopy measured in the TEM on individual nanoplatelets (inset) reveals the presence of P and O elements, whereas, C and Cu contribution was from the TEM grid. To quantify this, the atomic ratio of oxygen to phosphorus (O/P) was measured by EDAX in individual nanoplatelets along with the individual platelet length. A total of 35 individual nanoplatelets were measured. As shown in Figure 3D, O/P scales inversely with the length of the nanoplatelet (L). This implies

smaller, thinner nanoplatelets have greater oxygen content as compared to the larger nanoplatelets.

As with other nanoplatelets such as FeS_2, we argue that this indicates that the oxygen atoms are localized on the nanoplatelet surface. Under these circumstances, we calculated that the O/P ratio should scale with L as:[40,68]

$$\frac{O}{P} = \frac{(N/A)_O \times 2(k_1 + k_2 + 1)}{(N/V)_P \times L} \qquad (3)$$

where $(N/A)_O$ is the number of O atoms per unit surface area of platelet, $(N/V)_P = 4.55 \times 10^{28}$ m^{-3}, is the number of P atoms per unit volume of platelet and $k_1 = 7$ and $k_2 = 2.2$ are the L/t and L/W aspect ratios of the platelets as measured by AFM. Fitting this equation to the data (dotted line in the Figure 3D), allows us to estimate $(N/A)_O = 6.2 \times 10^{19}$ m^{-2}, implying an average distance between O atoms of 1.3 Å. This value appears to be too small to be realistic. This implies that the O atoms are not localized exactly on the platelet surface but occupy a thin layer extending a small distance into the interior of the platelets. Further studies of spectroscopic metrics on the nanoplatelets can be found in Section SII, Figure S6, Supporting Information.

2.2. Application as Anodes for Na-Ion Battery

The first part of this paper described the production and characterization of quasi-2D nanoplatelets of red phosphorus. As shown by Tai et al.,[48] using very thin nanoplatelets of standard Li-storing materials in lithium-ion battery cathodes can yield remarkable improvements in the rate-performance and cyclability as compared their corresponding bulk forms. This is largely due to the reduced diffusion lengths in the nanoplatelets. Here, we will demonstrate that quasi-2D red phosphorous nanoplatelets can act as extremely high-performance sodium ion battery anodes superior to the best non-2D phosphorous-based materials in the literature.

As discussed in the introduction, we have repeatedly found that when Li-storing active materials are incorporated into electrodes in the form of 2D or quasi-2D particles, extremely high capacities can be achieved, especially if single-walled carbon nanotubes (SWCNT) are used in place of both conductive additive and polymeric binder.[69–71] Such an electrode architecture combines a highly conductive and mechanically strong SWCNT network to facilitate charge delivery allowing the maximizing of capacity, rate capability and cyclability.[27,40,41,72,73] We have no reason to believe that this will not also apply to Na-storing electrodes. Given the very high theoretical capacity of phosphorous, we expect composites of RP nanoplatelets and SWCNT to have great potential for use in high performance Na-ion batteries.

To test this proposal, we prepared anodes using the smallest size-selected nanoplatelet dispersion (2000–3600 g). The smallest fraction was selected because they are also the thinnest nanoplatelets with a mean thickness ≈22 nm and mean length ≈139 nm (Figure S2, Supporting Information). Such thin nanoplatelets have very short ion diffusion paths, as compared to other fraction of sizes, yielding the smallest solid-state diffusion times. This is expected to yield enhanced rate performance.[74]

Note that the average sizes of nanoplatelets in the smallest fraction is greater than 60 nm which is large enough to avoid parasitic reactions caused by small particles with high-surface area.[18,23] This nanoplatelet dispersion was mixed with IPA-dispersed SWCNT and vacuum filtered onto Celgard 2320 membranes to produce composite films with 19–21 wt% nanotubes (no polymeric binder), a total (P+SWCNT) mass loading of $M_T/A = 0.63$ mg cm^{-2} and a thickness of ≈6 μm (**Figure 4**A, refer to Section 4 for more details). The as-prepared free-standing vacuum filtered RP/SWCNTs composite films (Figure S7A, Supporting Information) were then cut into the required dimensions for electrochemical testing (area of the film, $A = 0.178$ cm^2). SEM cross-sectional measurements were carried out on such films and showed a porous network of red phosphorus nanoplatelets uniformly mixed with a well-dispersed SWCNT network (Figure 4A). From the thickness and mass loading data we can estimate the electrode density at ≈1073 kg m^{-3}. Given the densities of red phosphorous (2340 kg m^{-3}) and SWCNT (≈1800 kg m^{-3}), this is consistent with a porosity of ≈52%.

We first characterized the electrochemical properties of the RP/SWCNTs composite electrode using cyclic voltammetry (CV). Figure 4B shows five CV cycles measured on a fresh (without any prior activation) RP/SWCNTs electrode in the potential range of 0.05–2.5 V (vs Na$^+$/Na), measured at a scan rate of 0.1 mV s^{-1}. We expect these curves to correspond to the following redox process during sodiation and desodiation (P + 3Na$^+$ + 3e^- ↔ Na$_3$P). In the first discharge cycle, three broad cathodic peaks (c_i, c_{ii}, and c_{iii}) were observed at around 0.9, 0.27, and 0.1 V (vs Na$^+$/Na) respectively. The c_i peak at 0.9 V disappears in subsequent cycles and is most likely due to the formation of a solid electrolyte interface (SEI) on the RP/SWCNTs electrode surface.[75,76] In subsequent cathodic cycle, a small peak at around 1.0 V is observed and could be ascribed to the subsequent sodiation of RP/SWCNTs to form an alloy NaP$_7$[77] Furthermore, stepwise Na$^+$ ion insertion generates c_{ii} and c_{iii} peaks at 0.27 and 0.1 V, respectively, corresponding to the formation of different alloy phases (NaP and Na$_3$P).[78,79] From the first anodic cycle, three peaks (a_i, a_{ii}, and a_{iii}) can be observed at 0.54, 0.74, and 1.8 V, respectively, implying the stepwise de-sodiation from the fully charged Na$_3$P phase to form intermediates of NaP, Na$_3$P$_{11}$, and P according to the Na-P phase diagram.[80]

Next, we quantify the Na-storage capacity of these composite electrodes. We performed galvanostatic charge–discharge (GCD) measurements on RP/SWCNTs electrodes. Unless otherwise stated, both discharge capacity and current density were calculated based on the weight of the active material and expressed as Q/M_{Act}. Initial results showed that applying a standard 5-cycle, and low current (at 625 mA g^{-1}) cycling process yielded electrodes (refer to Figure S7B, Supporting Information) which displayed very serious capacity fade (losing ≈80% of capacity over first ≈75 cycles). This is due to either slight pulverization of RP nanoplatelets that are not entirely wrapped by carbon nanotubes,[81] or formation of alloy intermediates in the de-sodiation steps as explained in Section SIIIa, Supporting Information. However, after measuring rate performance, when the current density was reduced back to 625 mA g^{-1}, the capacity was increased as compared to the initial capacity observed at the same current density prior to the rate performance (refer Figure S7B, Supporting Information).
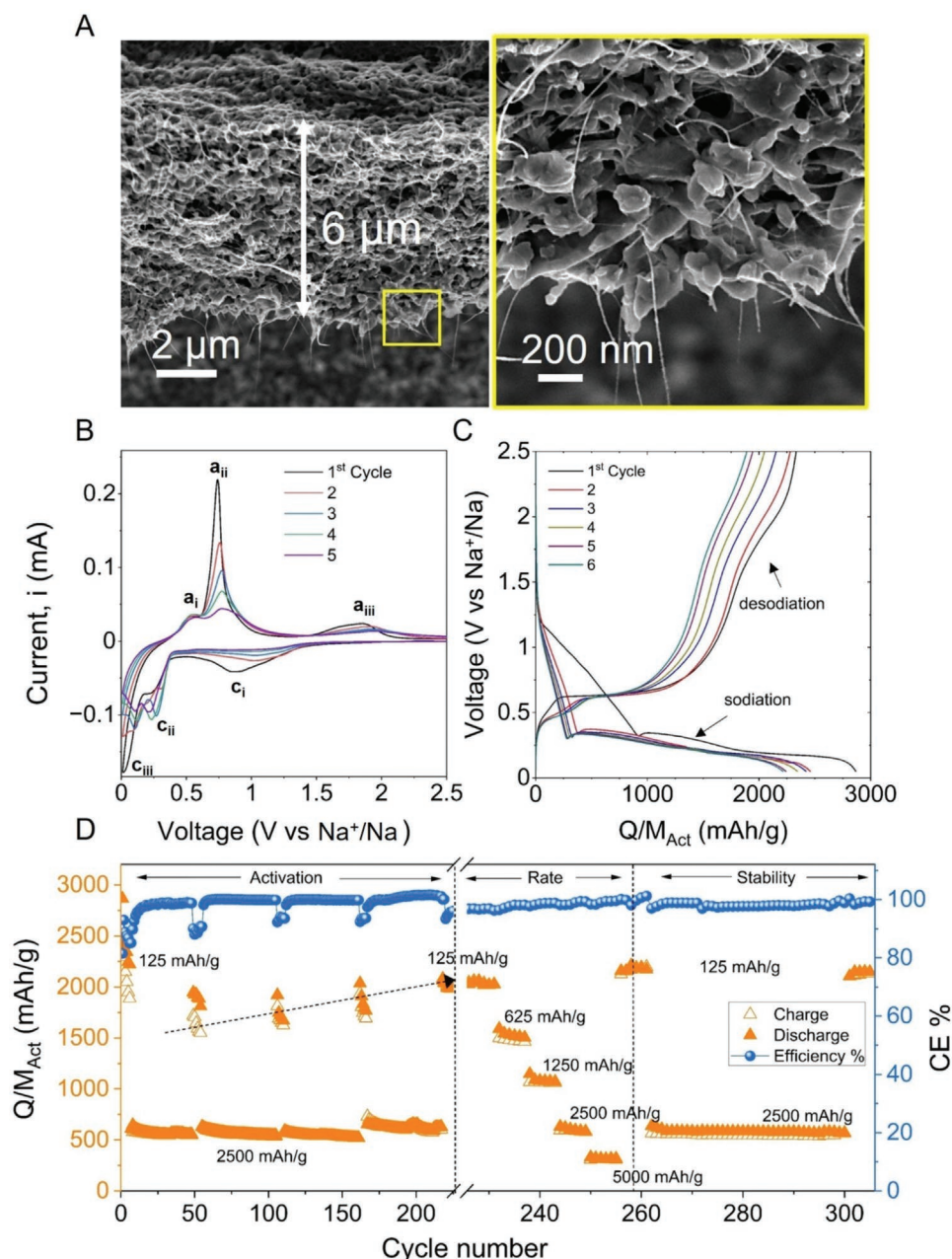
Figure 4. Electrochemical performance of RP/SWCNTs composites as Na-ion battery anodes ($M_f^{CNTs} = 20\%$, $A = 0.178$ cm^2, $M_T/A = 0.63$ mg cm^{-2}). A) Cross-section SEM image of RP/SWCNTs composite film with mean thickness of 6 μm. The higher magnified SEM image shows a uniform distribution SWCNT with RP nanoplatelets. B) Cyclic voltammograms curves of RP/SWCNTs composite anode for the first 5 cycles at a scan rate of 0.1 mV s^{-1}. C) The first five consecutive galvanostatic discharge–charge voltage profiles at a current density of $I/M_{Act} = 125$ mA g^{-1}. D) Galvanostatic charge–discharge cycling results for a RP/SWCNTs composite electrode exposed to an extended activation process (cycles 1–225) comprising two different current densities 125 mA g^{-1} (for 6 cycles) and 2500 mA g^{-1} (for 50 cycles) repeated four times, followed by a rate performance measurement (cycles 226–261), followed by a stability measurement (cycles 262–305). All specific capacities and currents are normalized to the mass of the RP. The blue data points indicate the CE % as a function of cycle number.

We believe the observed increase in the capacity (Figure S7B, Supporting Information) is due to an activation process which is more effective at high current.

This inspired us to develop an extended activation process with the aim of producing stable, high-capacity electrodes. To achieve this, we initially applied 6 low-current

($I/M_{Act} = 125$ mA g^{-1}) activation cycles, followed by 40–50 high-current cycles ($I/M_{Act} = 2500$ mA g^{-1}). This pattern was then repeated 4 times. The function of the high-current cycles is to achieve high-rate activation and also to reduce the activation time. The purpose of the low-current cycles is to act as a "probe" to allow us to see if the low-current capacity increases

**ADVANCED
SCIENCE NEWS**

www.advancedsciencenews.com

**ADVANCED
ENERGY
MATERIALS**

www.advenergymat.de

with activation. After this process, we performed a rate-performance measurement to allow the analysis of the activated electrode followed by continued cycling at high current to check the stability of the activated electrode.

Shown in Figure 4C are voltage profiles associated with the first six low current ($I/M_{Act} = 125$ mA g^{-1}) activation cycles. These initial cycles are similar to a standard activation procedure which allows the SEI layer to form on the electrode surface.[76] The charge/discharge voltage plateaus are consistent with the redox peak potentials in CV curves shown in the Figure 4B (see Figure S8, Supporting Information, for differential voltage plateaus).

The capacity results extracted from the GCD curves obtained during extended activation, followed by rate and stability measurements are shown in Figure 4D. We first describe the extended activation regime (cycles 1–225). Cycle 1 shows very high initial discharge and charge capacities of 2866 and 2335 mAh g^{-1} respectively with coulombic efficiency (CE) of 81%. This initial irreversible capacity loss is mainly originated from the utilization of Na$^+$ ions in the formation of the SEI.[82] Over the next five activation cycles, the reversible discharge capacity gradually decreased from 2467 to 2221 mAh g^{-1} while the CE rose to 89%. When the current was increased to 2500 mA g^{-1}, good cycling performance is observed, with a stable capacity of 565 mAh g^{-1}. After 20 cycles of this regime, the coulombic efficiency was >99%. On the 56th cycle the current was reduced to 125 mA g^{-1} again resulting in a sharp increase in capacity, note that the low coulombic inefficiencies (90%) were observed, partially due to the irreversible insertion of Na-ions into the amorphous RP/SWCNTs composite electrode at low rates. This is followed by a sharp capacity reduction when the current was returned to 2500 mA g^{-1}. This pattern was repeated for cycles 106 to 161 and again for cycles 162 to 217. The capacity and CE are remaining quite stable when electrodes cycling at a high current density up to 225 cycles of the activation process.

The important result here is that, during the extended activation process, the capacity obtained at high current (2500 mA g^{-1}) was very stable at ≈550–600 mAh g^{-1}. However, during the low-current "probe" cycles, the measured capacity increases with cycling (charge capacity increasing from ≈1600 to 2000 mAh g^{-1}, see arrow), while the capacity stabilizes with the results becoming more repeatable and the charge and discharge capacity converging. By the end of the extended activation process (cycle 226), the low-current capacity has reached 2040 mAh g^{-1}, roughly 80% of the theoretical value.

Remarkably, the coulombic efficiencies approach 99.7% in 256th and 302nd cycles when the current was reduced to 125 mA g^{-1} after cycling at high rates in the extended activation and rate performance. This shows extended activation process improves both the CE and low-rate capacities. As explained in Section SIII b, Supporting Information, in detail, this is due to the formation of different intermediate alloys that form at the de-sodiation steps at low-rates. However, no such intermediate alloy formation takes place at high-rates resulting in a rapid desodiation process (Figure S8, Supporting Information).

To test the rate capability after extended activation, the composite electrode was further cycled at current densities from 125 to 5000 mA g^{-1} (Figure 4D from 230 to 260 cycles). As is typical during rate performance measurements, the capacity fell off as the current was increased, reaching 315 mAh g^{-1} when measured at a current of 5000 mA g^{-1}. After returning to 125 mA g^{-1}, the capacity increased to 2180 mAh g^{-1}. We will analyze the rate performance in more detail below. After the rate performance measurement, we tested the stability of the activated electrode by cycling at current densities of 2500 mA g^{-1} up to 300 cycles. The electrode displayed stable discharge capacities of 580 mAh g^{-1} over 280 cycles. Finally, after switching back to 125 mA g^{-1}, a stable high discharge capacity of 2150 mAh g^{-1} was recovered, indicating the outstanding stability of the activated RP/SWCNTs composite electrode. The regular long-term cyclic stability of RP/SWCNTs electrode at a current density of 2500 mA g^{-1} for 1000 cycles was also tested which revealed superior high cyclic stability of electrodes (refer to Section SIIIc, Figure S9, Supporting Information).

It should be pointed out that the extended activation process described above is quite time consuming and probably not practical for use with real batteries. However, at the lab scale this technique is extremely useful for achieving the maximized capacity in electrodes such as these.

2.2.1. Analysis of Performance after Extended Activation

To put these results in context, we compare the rate performance data (after activation, extracted from Figure 4D) with literature data for RP-based Na-storing electrodes in **Figure 5**A (all data sets collected from the literature are listed in Table S1, Supporting Information). For both the literature data and the data collected in this work, this graph shows both capacity and current normalized to the total electrode mass (including both P and additive masses), Q/M_T. This is to allow a fair comparison of actual performance given that many papers on phosphorous electrodes use very high proportions of conductive additives and so while the specific capacity when normalized to active mass appears high, the usable specific capacity can be quite low.

Because the composites in this work used only 20wt% SWCNT and no other additives, the total-mass-normalized capacity measured at 100 mA g^{-1} was high, more than 1700 mAh g^{-1}. To our knowledge this is higher than any other phosphorous based electrode and higher than any 2D electrode material storing either Li or Na. In addition, the electrodes in this work show higher Q/M_T for all currents up to 1000 mA g^{-1}. However, for higher currents, our electrodes perform below the state-of-the-art, for example displaying 240 mAh g^{-1} at 5000 mA g^{-1} compared to the best literature values of 610 mAh g^{-1} at similar currents.[83] Taken together, these data show that, when post-activated, in quasi-2D form and combined with SWCNT, our electrodes have very high low-rate capacity implying very effective delivery of both Na ions and electrons to every part of the electrode. In addition, as shown in Figure S10, Supporting Information, comparison of these results with literature values for red phosphorus suggest 20% carbon nanotubes to be a near optimized additive formulation. However, the poor performance at high currents means the delivery of those ions and electrons is slower than for other phosphorous based anodes.

In order to understand the capacity results in Figure 5A, it is worth examining the effect of extended activation on electrode
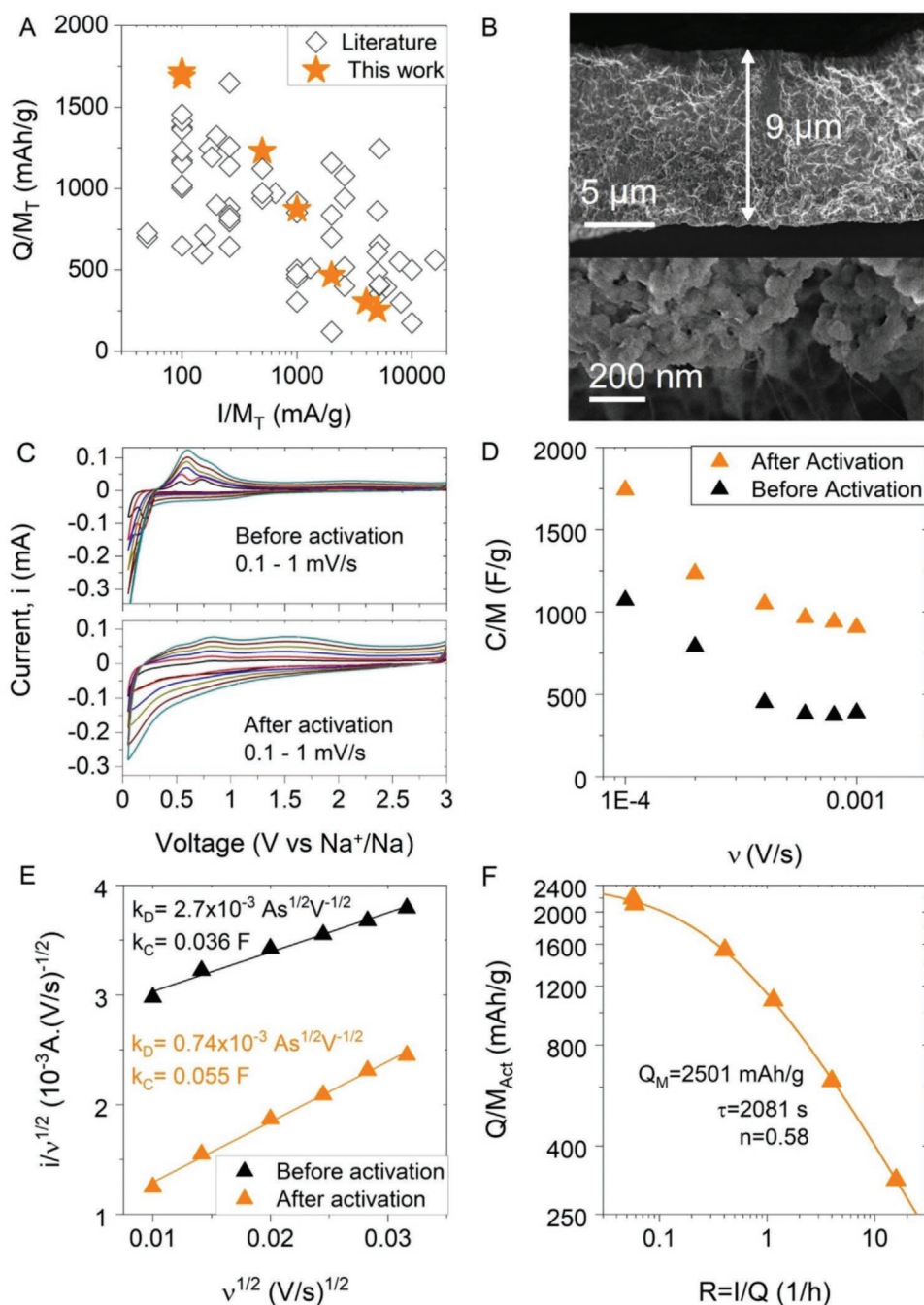
Figure 5. Effect of an extended activation on the performance of RP/SWCNTs composite electrode (M_f^{CNTs} = 20%, A = 0.178 cm^2, M_T/A = 0.63 mg cm^{-2}). A) Comparison of specific capacity versus current data obtained for RP/CNT composite electrode in this work to previous literature data. Here, capacity and currents are normalized to the total composite mass for comparison. B) Cross section SEM image of the RP/SWCNTs composite electrode after extended activation processes of 225 cycles and a high magnified image showing nanoplatelets with SWCNT. C) CV curves collected at various scan rates from 0.1 to 1 mV s^{-1} both before (after SEI formation cycles) and after the extended activation processes. D) Specific capacitance (calculated from the area enclosed by the CV curves) plotted versus scan rate for a RP/SWCNTs composite electrode before and after activation. E) Plot of $i_p/v^{1/2}$ versus $v^{1/2}$ for RP/SWCNTs composite electrode before and after activation with values of the capacitive (k_C) and diffusive (k_D) components shown (i_p measured at 0.52 V). F) Specific capacity plotted versus rate, R ($R = (I/M_{Act})/(Q/M_{Act})$) for a post-activation electrode. The fit is to Equation (2) with the fit parameters given in the panel.

structure and properties. We start by examining SEM cross section images of the RP/SWCNTs composite electrode after 306 cycles (Figure 5B), which can be compared to the pre-activation image in Figure 4A. First, these images indicates that the electrode has expanded from the thickness of 6 µm to 9 µm after activation and clearly show a morphological change after cycling. Although nanotubes are still visible, well-defined particles are no longer clearly seen. This thickness increase implies a reduction of density from 1050 kg m^{-3} before activation to 700 kg m^{-3} after activation implying an increase in porosity from 52% to 68%.

Second, although Figure 5B shows the presence of the SWCNT network, the morphology of the phosphorous appears significantly different to that shown in Figure 4A. After activation, the electrode appears much smoother with no platelets visible, implying a morphological change to a more uniform, amorphous structure. Post-mortem ex situ XRD measurements on an activated electrode (after 225 cycles, Figure S11, Supporting Information) were very similar to pre-activation diffraction spectra of the electrode, confirming the preservation of red phosphorus and carbon nanotubes in the composite electrodes after prolonged cycling. The EDAX spectrum (Figure S12, Supporting Information) also confirmed that the chemical compositional has not changed on post cycling as the electrode consist of P (O, P, and F atoms obtained from electrolyte) in similar proportions as before.

We further investigate the charge storage mechanism within the RP/SWCNTs composite electrodes, by performing CV curves at different scan rates before (after 6th cycle) and after extended activation (after 225th cycle) (Figure 5C). The curves before activation are reasonably consistent with the early cycle CVs shown in Figure 4B and show increasing current as scan rate, v, increasing from 0.1 to 1 mV s^{-1}. After activation, the CV curves are much broader and relatively featureless, possibly due to morphological changes upon activation but also perhaps due to increased double layer nature of the charge storage.[84] The specific capacitance of the RP/SWCNTs composite electrodes before and after activation was calculated for each scan rate from the area under the CV curve. Figure 5D presents the specific capacitance of the composite electrodes before and after activation as a function of scan rate ranging from 0.1 to 1 mV s^{-1}. Significantly, the activated electrode displays considerably higher capacitance at all scan rates. In the intrinsic, low-rate region, the specific capacitance is approximately 60% larger after activation. All other things being equal, this implies that the internal surface area of the RP/SWCNTs composite electrode is increased significantly after activation, consistent with the discussion above (refer to Figure S13, Supporting Information, for EIS).

We can analyze the CV data in more detail by assuming the current has both diffusion- and capacitance-limited components such that the peak current (0.54 V) is given by

$$i_p = k_C v + k_D v^{1/2} \tag{4}$$

with the subscripts indicating the capacitive and diffusive components.[85] We plot the data as $i_p/v^{1/2}$ versus $v^{1/2}$ in Figure 5E. We find good linearity demonstrating the validity of this equation with fitting yielding values of k_C and k_D as shown in the

Figure 5E. This plot shows that while the before-activation sample is heavily diffusion limited, after activation the electrodes are somewhat more capacitance-limited.

2.2.2. Quantitative Rate-Performance Analysis

We can study the performance of these post-activation electrodes in a more quantitative manner by analyzing the rate performance. To do this, we plot the measured specific capacity (Q/M_{Act}) (normalized to RP mass, i.e., not including the CNT mass) versus the rate parameter, R, which is defined via $R = I/Q$, that is, the ratio of the current to the stored charge.[31,86–89] This parameter is useful because $1/R$ is a measure of the actual charge/discharge time of the electrode at constant current. In addition, plotting the capacity normalized to active mass (rather than total mass) allows one to assess the performance of the RP as enabled by its morphology as well as electrode architecture (thickness, nature of additives, etc.). This data shows the measured capacity to fall off with rate as is generally observed.[89,90] However, at low rate, Q/M_{Act} is very high, reaching 2240 mAh g^{-1}. To our knowledge the only two papers have shown higher low-rate Q/M_{Act} than this, 2570 (ref. [10]) and 2654 (ref. [91]) mAh g^{-1}. However, in both cases, achieving these values required much higher levels of additive (30 wt% and 77.4 wt%, respectively) than used here (20 wt%). Higher additive contents mean lower percentage active mass which leads to relatively low values of Q/M_T.

We perform the rate-analysis by fitting this data, using a semiempirical equation proposed recently by us:[89]

$$Q/M_{Act} = Q_{M,Act} \left[1 - (R\tau)^n \left(1 - e^{-(R\tau)^{-n}} \right) \right] \tag{5}$$

Such fitting can yield three fit parameters: $Q_{M,Act}$, which is the specific capacity (normalized to active mass) at very low rate, a parameter that can be compared to the theoretical capacity; τ, the characteristic time associated with charge/discharge; and n, a parameter whose value indicates the dominance of diffusive ($n = 0.5$) or capacitive/electrical ($n = 1$) limitations on rate performance.[31,86,87,89,90] As shown in Figure 5F, this equation fits the data extremely well. The obtained fit values were $Q_{M,Act} = 2501$ mAh g^{-1}, $n = 0.58$, and $\tau = 2081$ s.

The value of $Q_{M,Act} = 2501$ mAh g^{-1} represents the achievable capacity at very low rate and is actual measure of the performance of the active material within the electrode. This value is very close to the theoretical value of ≈2600 mAh g^{-1} indicating that 96% of the phosphorous in these electrodes are reversibly storing sodium. The values of τ and n will be discussed below as part of our study on the effect of electrode thickness on rate performance.

2.2.3. Thick Electrodes

Up to this point we have studied thin (≈9 µm post-activation), phosphorus-based electrodes in order to best assess their ultimate performance. However, real battery electrodes tend to be much thicker than this, perhaps up to 100 microns thick.

There can be many difficulties associated with producing thick electrodes using novel materials, for example cracking during solution-based electrode fabrication.[33] In addition, the specific electrode capacity tends to fall somewhat as electrode thickness is increased while the rate performance almost always degrades as electrode thickness is increased.[92] Here we investigate the

Figure 6. Thickness dependence of RP/SWCNTs composite electrodes (M_f^{CNTs} = 20%, A = 0.178 cm², M_T/A = 0.63–10.74 mg cm⁻²). A) Cycling data including activation regime (1–200 cycles), rate performance measurement (200–250 or 200–280 cycles depending on sample) and stability measurement (>250 or >280 cycles depending on sample) for composite electrodes of two different post-activation thicknesses, 9 and 135 µm. B) Rate performance data plotted as areal capacity versus areal current for four electrode thicknesses (post-activation). The lines plot constant charging times. C) Data from B plotted as active-mass-normalized capacity versus rate, R ($R = Q/I$). the lines are fits to Equation (2). Fit parameters extracted from fits in (C), all plotted versus post-cycling electrode thickness. These parameters represent the low-rate, D) active-mass-normalized capacity, $Q_{M,Act}$, E) low-rate areal capacity, Q_A, F) the exponent, n, which describes the decay of capacity with rate and G) the characteristic time associated with charge/discharge, τ. The data in (E) was obtained by rescaling the data in (D) to represent the low-rate areal capacity, first converting from active mass-normalized data to total-mass-normalized data and then to areal capacity, Q_A: $Q_A = Q_{M,Act}(1 - M_f) \rho_{electrode} L_E$. Also shown in E are data extracted from Table S2, Supporting Information, showing estimated values of areal capacity versus electrode extracted from published works. H) Figure of merit for rate performance, τ/L_E^2, plotted versus (post-activation) electrode thickness, L_E. The grey stars represent published data as reported in a recent review. The line represents a prediction by the model described in the text. Inset: Figure of merit for capacity-rate trade-off, τ/Q_A, plotted versus post activation electrode thickness.

performance of our phosphorus based composite electrodes when the thickness is increased beyond 100 microns.

We prepared three fresh composite electrodes with mass loadings of 2.4, 7.4, and 10.8 mg cm⁻² and (pre-activation) thicknesses of 22, 70, and 100 µm. We performed activation followed by rate performance and stability testing as before. Postmortem SEM analysis showed activation led to increases in electrode thickness to 38, 135, and 175 µm, respectively, yielding post-activation electrode densities of 640, 550, and 616 kg m⁻³ (porosities between 71%, 75%, and 72%). This capacity data obtained during activation/rate/cycling data is plotted as areal capacity versus cycle number in **Figure 6**A for the 38 and 135 µm thick electrodes (see Figure S14, Supporting Information, for 175 µm thick electrode). In all cases, activation resulted in a reasonably stable capacity. We analyze the rate performance of these electrodes by plotting their areal capacity as a function of areal current in Figure 6B (with the 9 µm thick (post activation) electrode from before shown for comparison). Here we find the areal capacity to increase significantly with electrode thickness due to the increased storage volume. The thickest electrode shows a measured maximum capacity of 10.0 mAh cm⁻² at 1.4 mA cm⁻². This value is extremely high, far higher than the highest areal capacity reported for a phosphorous based Na-storing electrode which was ≈1.7 mAh cm⁻².[10] It is also competitive with the highest areal capacities reported for Li batteries which are mostly in the 4–16 mAh cm⁻² range.[93] For context, commercial battery electrodes tend to store approximately 4 mAh cm⁻². In addition, we find that the thickest film displays a good combination of capacity and rate performance, for example displaying an areal capacity of 7.9 mAh cm⁻² can be achieved at areal currents of ≈7 mA cm⁻². This data would imply a charging time of 1 h, which is quite impressive for such a high capacity.

In order to quantitatively analyze the data, we plot Q versus R in Figure 6C for the 9, 38, and 175 µm thick samples (the 135 µm thick sample is not shown to avoid clutter). We then fit these datasets using Equation (2) to obtain $Q_{M,Act}$, τ, and n.

In Figure 6D, we plot $Q_{M,Act}$, the active-mass normalized capacity at extremely low rate, versus electrode thickness, L_E. We find that, while the 9 µm thick films display a $Q_{M,Act}$ value very close to the theoretical value, $Q_{M,Act}$ falls off with increasing thickness, reaching ≈1300 mAh g⁻¹ for the thickest electrodes. This fall-off in capacity with thickness is often observed,[94,95] especially for very thick electrodes. For low-rate capacity, it reflects the increasing difficulties in delivering charge and ions to every part of the electrode as the thickness increases.

However, we note that $Q_{M,Act}$ is not the main technologically relevant quantity. More important is the areal capacity, as this ultimately controls the energy density.[33] We use the data for $Q_{M,Act}$ to calculate the low-rate areal capacity, Q_A. We do this by first using the nanotube mass fraction (20%) to convert $Q_{M,Act}$ to the low-rate capacity normalized to total electrode mass. We then convert this to Q_A using the measured electrode thickness (L_E) and density. The resultant values of Q_A are plotted versus L_E in Figure 6E. Although the resultant values are lower than would be achieved if $Q_{M,Act}$ remained close to theoretical values at all thicknesses, we still observe Q_A to increase strongly with thickness, reaching 10 mAh cm⁻² for the 175 µm thick electrode, a very high value for Na ion batteries. For comparison,
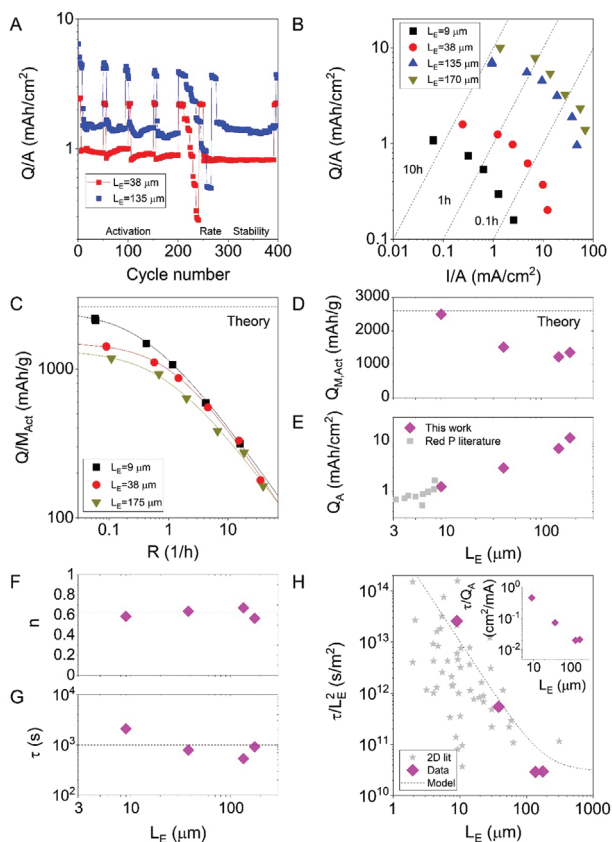
this figure also shows literature values for RP-based anodes extracted from Table S1, Supporting Information. We reiterate that our best value is far higher than the highest areal capacity reported for a phosphorous based Na-storing electrode which was ≈1.7 mAh cm^{-2}.[10] As mentioned above, values of low-rate areal capacities above 10 mAh cm^{-2} are rare, even for lithium-ion batteries.[10,27,33]

However, because achieving very high areal capacities generally requires high electrode thicknesses, they are usually accompanied by poor rate performance.[86,89] This is primarily because the time scale associated with ionic diffusion within the electrolyte filled pore network increases strongly with electrode thickness, leading to reduced rate performance in thicker electrodes.[86,89] This makes it very important to carefully analyze rate performance especially in thick electrodes. Shown in Figure 6F is a plot of rate exponent, n, versus electrode thickness. This parameter value indicates the dominance of diffusive ($n = 0.5$) or capacitive/electrical ($n = 1$) limitations on rate performance.[31,86,87,89,90] In our electrodes, n does not vary significantly with electrode thickness, lying between 0.56 and 0.68 in all cases (mean = 0.63, dashed line). This indicates that these electrodes are predominantly limited by diffusion with a minor capacitive contribution.

In Figure 6G, we plot the characteristic time, τ, associated with charge/discharge. The longer τ is, the worse the rate performance. In general, τ always increases with electrode thickness because of the dependence of factors such as in-pore diffusion on thickness.[86,89] Because τ can never decrease with L_E, the best one can hope for is τ to stay roughly constant with L_E, as might occur if, for example, the rate performance were predominantly limited by solid state diffusion.[86,89] Although it is slightly scattered, the data in Figure 6G shows τ to be roughly constant with L_E, with a mean value of ≈1000 s. It is extremely unusual that τ should be constant with electrode thickness up to thickness is as high as 100 µm. Indeed, according to a recent review on rate performance in both Na and Li ion storing electrodes published by our group, values of τ of ≈1000 seconds would expected for electrodes with thickness in the 100–200 µm range.[89] Conversely, thin electrodes below 10 microns would be expected to have τ-values between 1 and 10 s.

To understand this unusual behavior, it is necessary to consider a physical model for τ. Previously, we proposed a model which expresses τ in terms of various contributions from various capacitive and diffusive processes.[89] Since then, we have reported a significant amount of data demonstrating that this model describes a wide range of rate performance experiments for Li and Na ion batteries.[31,86,87,92] This model leads to an equation for τ which can be expressed as (see Section SV, Supporting Information):

$$\tau = 28Q_V \underbrace{\left[\frac{L_E^2}{2\sigma_{OOP}} + \frac{L_E^2}{2\sigma_{BL}P_E^{3/2}} + \frac{L_E L_S}{\sigma_{BL}P_S^{3/2}} \right]}_{\text{Capacitive (resistive) terms}} + \underbrace{\left[\frac{L_E^2}{D_{BL}P_E^{3/2}} + \frac{L_{AM}^2}{D_{AM}} \right]}_{\text{Diffusive terms}} \quad (6)$$

(see ref. [89] for a detailed description of the meaning of the terms). Here Q_V is low-rate volumetric capacity of the electrode, σ_{OOP} is the out-of-plane[31] electronic conductivity of the electrode, P_E and P_S are the porosities of the electrode and separator

respectively while L_S is the separator thickness. Also, σ_{BL} is the overall (anion and cation) ionic conductivity of the bulk electrolyte (S m^{-1}) while D_{BL} is the ion diffusion coefficient in the bulk electrolyte. In addition, L_{AM} is the solid-state diffusion length associated with the active particles (related to particle size); D_{AM} is the solid-state Li ion diffusion coefficient within the particle.

The only term in this equation that does not depend on the electrode thickness, L_E, is the final term, which describes the timescale associated with solid state diffusion (τ_{SSD}) of Na ions within the RP platelets. The fact that τ appears to be L_E-independent within this thickness range implies this term to be dominant over the other terms in this equation. This means that to a first approximation:

$$\tau \approx \tau_{SSD} = \frac{L_{AM}^2}{D_{AM}} \quad (7)$$

If we estimate L_{AM} as half the mean original nanoplatelet thickness (≈10 nm) and use the reported value for the diffusion coefficient of Na ions in RP ($D_{AM} = 10^{-19}$ m^2 s^{-1}),[12] the solid state diffusion time is $\tau_{SSD} \approx 1000$ s, which is very good agreement with the data in Figure 6G (dashed line). This implies that, for electrode thicknesses up to 100 µm, τ is completely dominated by solid diffusion within the RP platelets. This is quite unusual as one or more of the other terms in Equation (4) usually dominate in thick electrodes, leading to super-linear increases in τ with L_E.[86,89] The reason that this does not occur here is that the solid state diffusion coefficient for RP is extremely small, leading to very slow diffusion. For comparison, a recent survey[90] of solid state diffusion coefficients in 2D materials found D_{AM} values between 10^{-13} and 10^{-19} m^2 s^{-1} making RP comparable with the most sluggish quasi-2D materials.

While the parameter τ contains information about the rate performance of battery electrodes, it is not a good figure of merit (FoM) for rate performance due to its strong dependence on electrode thickness. Previously, we have proposed that a better FoM is[90] τ / L_E^2 (or even L_E^2 / τ),[89] which can be found from Equation (4):

$$\frac{\tau}{L_E^2} = 28Q_V \left[\frac{1}{2\sigma_{OOP}} + \frac{1}{2\sigma_{BL}P_E^{3/2}} + \frac{L_S}{L_E \sigma_{BL} P_S^{3/2}} \right] + \left[\frac{1}{D_{BL}P_E^{3/2}} + \frac{L_{AM}^2}{L_E^2 D_{AM}} \right] \quad (8)$$

This parameter is useful as, for the large values of L_E associated with commercial electrodes, the third and fifth terms become very small, yielding a constant value of τ / L_E^2 which can be used as an FoM to represent rate performance. Smaller values of τ / L_E^2 indicate better rate performance with the very best performing electrodes displaying $\tau / L_E^2 \approx 10^9$ s m^{-2}.[89]

As shown in Figure 6H, we plot τ / L_E^2 versus L_E for our RP/SWCNT electrodes. For comparison, we also plot data for a range of other 2D Li or Na storing materials (grey stars) as extracted from a recent review.[90] It is clear from this graph that both our values and literature data show a falloff in τ / L_E^2 with increasing L_E. This is in line with Equation (8) where the third and fifth terms decrease with increasing L_E. Interestingly, for small values L_E our data is at the upper end of the spread in literature values, consistent with relatively

**ADVANCED
SCIENCE NEWS**

www.advancedsciencenews.com

**ADVANCED
ENERGY
MATERIALS**

www.advenergymat.de

poor rate performance. However, for $L_E > 100$ µm, our values ($\tau / L_E^2 \approx 3 \times 10^{10}$ s m^{-2}) are in line with the lowest literature values consistent with rate performance at the state-of-the-art for 2D materials.

In order to test whether these results are in line with expectations, we use Equation (8) to model the dependence of τ / L_E^2 on L_E for our RP/SWCNT electrodes. We do this by using values for the various parameter which are either extracted from the data above or estimated from the literature (see Table S2, Supporting Information). In this way, we obtain the dashed line in Figure 6H which matches the experimental data very well. We note that this curve saturates at high L_E (as mentioned above) at a constant value very close to our best (lowest) experimental values of τ / L_E^2. This shows that our $L_E > 100$ µm electrodes display the maximum achievable rate performance for this system.

Finally, it is worth considering the simultaneous optimization of capacity and rate performance. Thin electrodes tend to display good rate performance (low τ) but poor areal capacity (low Q_A). Alternatively, thick electrodes usually display poor rate performance (high τ) but good areal capacity (high Q_A). In order to obtain a reasonable combination of rate performance and areal capacity, an intermediate thickness is required. Previously, we argued that's the best tradeoff between areal capacity and rate performance is achieved when the parameter τ/Q_A is minimized.[88] To investigate this, we plot τ/Q_A versus electrode thickness (L_E) in Figure 6H inset. We find that τ/Q_A falls with increasing electrode thickness, reaching a value of 0.02 for our thickest electrodes. This is close to the minimum possible value of 0.01 as revealed by modeling.[88] These results indicate that not only do our thickest electrodes have high areal capacity and excellent rate performance what does this combination of values is close to the best possible capacity rate tradeoff.

It is worth noting that, although we have achieved extremely high-performance electrodes, our nanoplatelets are not fully optimized with regard to size. For example, while thin nanosheets yield very short solid-state diffusion paths, they also lead to extremely high internal surface areas which can lead to parasitic side reactions and consume a large amount of sodium in the formation of the SEI. Thus, it is likely that there is an optimized platelet thickness which yields the most effective balance of these two factors. Future works will study the effect of nanoplatelets size on battery performance in order to achieve better optimization at a materials level.

3. Conclusion

In this manuscript, LPE was used to synthesize the 2D-form of red phosphorus. The resultant nanoplatelets were found to be amorphous, with aspect ratio varying between 3 and 18. These nanoplatelets are reasonably air stable but display low level of oxidation on the surfaces. Stable, high-performance sodium storing battery electrodes have been produced by mixing these RP nanoplatelets with carbon nanotubes followed by an extensive activation process. The electrodes show extremely high capacity and a reasonably good rate performance. Thick electrodes with thickness up to 175 microns were produced and it was found that they can store almost 10 mAh cm^{-2} and be charged in approximately 1 h. We believe this work will pave the

way to explore more novel nanoplatelets of Na-storing materials to replace the Li-storing batteries in near future.

4. Experimental Section

Liquid Phase Exfoliation: Red phosphorus solids (99.99%, 7 723 140) were purchased from Sigma-Aldrich. P3-SWCNT was purchased from Carbon Solutions (carbonaceous purity > 90%). Solvents, *N*-methyl-2-pyrrolidone and 2-propanol were purchased from Sigma-Aldrich HPLC grade > 99%.

Red phosphorus dispersion was prepared by probe-sonication of the solids in the solvent, *n*-methyl-2-pyrrolidone (NMP). An initial concentration of 15 gL^{-1} was used as the starting concentration. First, the solids (~1200 mg) was immersed in 0.2 mL NMP, in a 100 mL metallic beaker, and then crushed into smaller chunks (images are shown in Figure S1, Supporting Information). NMP solvent was then added into it to make it a total of 80 mL. The mixture was then subjected to probe sonication using a horn probe tip (VibraCell VCX, 750 W) for time period of 10 h at 55% amplitude with pulse 6 s on-2 s off, under ice-cooling. After probe sonication, the dispersion was first centrifuged at g-force of 100 *g* for 2 h in 40 mL aliquots by using 50 mL vials in a Hettich Mikro 220R centrifuge. The centrifuge has a fixed-angle rotor of radius 91 mm. The sediment containing the unexfoliated and thicker products were discarded, and the supernatant consisting of exfoliated material is subjected to a second centrifugation at 3660 *g* for 3 h. After this step, the supernatant was discarded, and the sediment with some residual NMP solvent was washed further to remove the NMP residual solvent in the dispersion as much as possible, and to re-disperse the exfoliated nanoplatelets in IPA. For washing step, first the sediment obtained after 3660 g along with some residual solvent NMP was subjected to a high-speed centrifuge at 32 kg for 20 min in small 1.5 mL Eppendorf. This step ensures the sediment was well settled at the bottom of the Eppendorf and the supernatant consisted of degraded NMP was discarded. 1 mL of IPA (1 mL in each 1.5 mL Eppendorf) was then added in each Eppendorf containing the sediment and was subject to a centrifugal force of 32 kg for 10 min. After this step, the supernatant was discarded again to ensure the removal of NMP solvent residues as much as possible from the sediment. The final sediment is then extracted, and bath sonicated for 10 min in 80 mL of IPA to obtain a dispersion called as standard sample (std-RP).

Liquid-cascade centrifugation was used for the size-selection of the as-obtained nanoplatelets of RP. The centrifugal force was expressed in units of *g* (acceleration due to gravity). All centrifugation steps in the experiment were performed at 10 °C using Hettich Mikro 220R centrifuge. After probe sonication, the unexfoliated material was removed by centrifuging the dispersion at 100 *g* for 2 h. The sediment was discarded, and the supernatant was subjected to a second centrifuge force at 400 *g* for 2 h. The supernatant and sediment obtained after this step was separated out carefully. The supernatant was further centrifuged at 1000 *g* for 2 h. Similar protocol was repeated by separating the sediment and supernatant again, producing the second sediment. Same procedure was repeated for the centrifugal forces 2000 *g* and 3660 *g*, thus producing four different sediments from the stock dispersion. The mass of the last sediment obtained after 3660 *g* was very low so no further size selection were done. Therefore, the final supernatant after 3660 g step was discarded. After all, 4 different size-selected sediments were obtained, around 5 mL of IPA is added in each sediment and bath sonicated for 10 min, resulted in 4 different sizes of dispersion. For washing step to ensure complete removal of NMP residual solvent, all four of these dispersions were filled in 1.5 mL Eppendorfs to a volume of 1 mL, and subject to a high-speed centrifuge at 32 kg for 10 min. This step ensures that if any NMP solvent residues were present in the sediments, it separates out from the sediment as a supernatant with IPA. The supernatants were discarded after this step, and the sediments of each size were again re-dispersed in IPA by 10 min bath sonication to get a total of 4 different size of dispersions. It was named as the

ADVANCED
SCIENCE NEWS
www.advancedsciencenews.com

ADVANCED
ENERGY
MATERIALS
www.advenergymat.de

largest dispersion (100–400 g), second largest (400–1000 g), third largest (1000–2000 g), and the smallest dispersion (2000–3660 g).

Formation of Composite Electrodes: Nanotube (SWCNT) dispersions were prepared with a concentration of 0.1 mg mL^{-1} by adding 8 mg of P3-SWCNT to 80 mL IPA and sonicating for 3 h using a horn-tip sonic probe (Vibracell CVX, 750 W) at 50% amplitude with an on/off pulse ratio of 6 s/2 s under ice cooling. To fabricate electrodes, the smallest size-selected dispersion of RP (2000–3660 g) in IPA was mixed with SWCNTs (80:20 by weight) dispersions in IPA by bath sonication for 10 min, and vacuum filtered on Celgard 2320 (thickness 20 µm) membrane with an area of 2 cm^2. The film was dried in ambient to obtain free-standing films (as shown in Figure S7, Supporting Information). Here, SWCNTs were used to maximize both the mechanical stability and electrical conductivity of the resulting films and were the only additives used. The resulting films were cut into the required dimensions for electrochemical testing ($A = 0.178$ cm^2). The areal mass loading of RP in electrodes were 0.63–10.8 mg cm^{-2}, with 20 wt% SWCNTs and approximate thicknesses was varying from 6 to 100 µm.

Characterization: The UV–vis extinction and absorption measurements were carried out on Perkin Elmer Lambda 1050 spectrometer between 220 and 900 nm using quartz cuvettes with a pathlength of 4 mm. The concentration of the dispersions was determined by filtration and weighing the membranes (Celgard 2320) for calculating the extinction coefficient. For the absorbance spectra, an integration sphere of radius 150 mm was used in the setup.

TEM imaging was performed using JEOL 2100, on Holey carbon grids (400 mesh), at an accelerating voltage of 200 KV. The EDX spectrum was acquired using 80 mm^2 X-Max EDAX detector from Oxford instruments attached to JEOL 2100. High resolution TEM and SAED were performed on FEI TITAN microscope. The high-angle annular dark field imaging was carried out at 300 KV.

XRD spectra were captured using a Bruker D8 discover high-resolution diffractometer with a Cu tube emitting K$_\alpha$ radiation (1.5406 Å) and a double-bounce Ge [220] monochromator. The spectra were acquired in the 2Θ range from 20° to 80° on the films prepared on the silicon (100) wafer.

Raman spectroscopy was performed using Horiba Jobin Yuon LabRAM ARAMIS instrument in ambient on bulk crystals and films of nanoplatelets. A 532 nm laser (laser power 2 mW, power is adjusted using neutral density filter) has been used to excite the samples with 10X objective. A grating of 1800 grooves mm^{-1} was used to disperse the signal onto the CCD detector at −70 °C. The samples for the Raman spectroscopy were prepared by drop-casting the dispersion (concentration ≈0.5 mg mL^{-1}) on pre-heated silicon wafers coated with 300 nm of silicon dioxide.

AFM was carried out on Bruker Multimode 8 microscope in ScanAsyst mode using OLTESPA R3 cantilevers. The wafers for the AFM were prepared by drop casting a diluted dispersion on heated Si/SiO$_2$ wafers at 80–100 °C and drying using argon gas.

The FTIR on the film of nanoplatelets was acquired using PerkinElmer spectrum 100 with csl optics in the range from 4000 to 400 cm^{-1}. The RP nanoplatelets/CNT composite films were imaged using a scanning electron microscope (Zeiss Ultra Plus). An accelerating voltage of 5 keV was used at a working distance of 5–6 mm with a 30 µm aperture.

Electrochemical Characterization: Half-cells were assembled using 2032 type coin cells (14 mm; MTI Corp.) in a glovebox filled with O$_2$ and H$_2$O content lower than 0.1 ppm and tested at room temperature. Sodium metal foil used as the counter/reference electrode, while Whatman glass fibre filters (GF10) was used as a separator. Sodium hexafluoridophosphate (NaPF$_6$, 1.2 м) in ethylene carbonate/dimethyl carbonate (EC/DMC, 1:1 in vol/vol, BASF) was used as the electrolyte with the 10 wt% fluoroethylene carbonates (FEC, Sigma-Aldrich) as an electrolyte additive. Cyclic voltammetry measurements were carried out using a galvanostat–potentiostat (VMP-3, Biologic) between 0.05 and 2.5 V versus Na$^+$/Na at a scanning rate of 0.1 mV s^{-1} for 10 cycles and also at different scan rates. Impedance measurements were performed using a Biologic VMP-3 with a frequency range of 1 MHz to 0.1 Hz and a voltage amplitude of 10 mV. EC-Lab Z-Fit software was used to model the acquired spectra. Using the GCD mode (Arbin), the electrochemical properties of the RP/SWCNTs anodes were measured within a voltage range of 0.05–2.5 V using a potentiostat.

The cyclabilities of the electrodes were evaluated at 625 and 2500 mA g^{-1} or 5000 mA g^{-1}. Electrodes were allowed to activate for the 6 initial formation cycles at 125 mA g^{-1}. After first 6 cycles, electrodes were cycled at high current density of 2500 mA g^{-1} for 50 cycles. For every 50 cycles activation at 2500 mA g^{-1} electrodes were cycle back to 125 mA g^{-1} for 5 cycles with 6 repetitive times, to check the capacity gains. Further, rate performance test was performed at various current rates (125, 625, 1200, 2500, 5000, and 6250 mA g^{-1}) for 6 cycles, later electrodes remain continued cycling at 2500 mA g^{-1} for 150 cycles to check the stability of the activated electrode and finally went back to 125 mA g^{-1} for 6 cycles to check the cells capacity at the end. And the coulomb efficiency was calculated from the ratio of charge capacity to discharge capacity. All specific capacities and currents are normalized to active material mass (M_{act}).

Supporting Information

Supporting Information is available from the Wiley Online Library or from the author.

Conflict of Interest

The authors declare no conflict of interest.

Data Availability Statement

The data that support the findings of this study are available in the supplementary material of this article.

[1] K. M. Abraham, *ACS Energy Lett.* **2020**, *5*, 3544.
[2] H. Pan, Y.-S. Hu, L. Chen, *Energy Environ. Sci.* **2013**, *6*, 2338.
[3] G.-L. Xu, R. Amine, A. Abouimrane, H. Che, M. Dahbi, Z.-F. Ma, I. Saadoune, J. Alami, W. L. Mattis, F. Pan, Z. Chen, K. Amine, *Adv. Energy Mater.* **2018**, *8*, 1702403.
[4] F. Yang, H. Gao, J. Chen, Z. Guo, *Small Methods* **2017**, *1*, 1700216.

[5] G.-L. Xu, Z. Chen, G.-M. Zhong, Y. Liu, Y. Yang, T. Ma, Y. Ren, X. Zuo, X.-H. Wu, X. Zhang, K. Amine, *Nano Lett.* **2016**, *16*, 3955.

[6] D. Hanlon, C. Backes, E. Doherty, C. S. Cucinotta, N. C. Berner, C. Boland, K. Lee, A. Harvey, P. Lynch, Z. Gholamvand, S. Zhang, K. Wang, G. Moynihan, A. Pokle, Q. M. Ramasse, N. McEvoy, W. J. Blau, J. Wang, G. Abellan, F. Hauke, A. Hirsch, S. Sanvito, D. D. O'Regan, G. S. Duesberg, V. Nicolosi, J. N. Coleman, *Nat. Commun.* **2015**, *6*, 8563.

[7] H. W. Lee, H. Jung, B. C. Yeo, D. Kim, S. S. Han, *J. Phys. Chem. C* **2018**, *122*, 20653.

[8] Y. Zhang, X. Rui, Y. Tang, Y. Liu, J. Wei, S. Chen, W. R. Leow, W. Li, Y. Liu, J. Deng, *Adv. Energy Mater.* **2016**, *6*, 1502409.

[9] W. Li, S. Hu, X. Luo, Z. Li, X. Sun, M. Li, F. Liu, Y. Yu, *Adv. Mater.* **2017**, *29*, 1605820.

[10] X. Liu, B. Xiao, A. Daali, X. Zhou, Z. Yu, X. Li, Y. Liu, L. Yin, Z. Yang, C. Zhao, L. Zhu, Y. Ren, L. Cheng, S. Ahmed, Z. Chen, X. Li, G.-L. Xu, K. Amine, *ACS Energy Lett.* **2021**, *6*, 547.

[11] J. Zhou, Z. Jiang, S. Niu, S. Zhu, J. Zhou, Y. Zhu, J. Liang, D. Han, K. Xu, L. Zhu, X. Liu, G. Wang, Y. Qian, *Chem* **2018**, *4*, 372.

[12] I. Capone, J. Aspinall, E. Darnbrough, Y. Zhao, T.-U. Wi, H.-W. Lee, M. Pasta, *Matter* **2020**, *3*, 2012.

[13] J. Zhou, X. Liu, W. Cai, Y. Zhu, J. Liang, K. Zhang, Y. Lan, Z. Jiang, G. Wang, Y. Qian, *Adv. Mater.* **2017**, *29*, 1700214.

[14] S. Liu, J. Feng, X. Bian, J. Liu, H. Xu, Y. An, *Energy Environ. Sci.* **2017**, *10*, 1222.

[15] J. Zhang, J. Gai, K. Song, W. Chen, *Cell Rep. Phys. Sci.* **2022**, *3*, 100868.

[16] Y. Fu, Q. Wei, G. Zhang, S. Sun, *Adv. Energy Mater.* **2018**, *8*, 1702849.

[17] G. Chang, Y. Zhao, L. Dong, D. P. Wilkinson, L. Zhang, Q. Shao, W. Yan, X. Sun, J. Zhang, *J. Mater. Chem. A* **2020**, *8*, 4996.

[18] J. Zhang, J. Qiao, K. Sun, Z. Wang, *Particuology* **2022**, *61*, 18.

[19] Y. Sun, N. Liu, Y. Cui, *Nat. Energy* **2016**, *1*, 16071.

[20] P. G. Bruce, B. Scrosati, J. M. Tarascon, *Angew. Chem., Int. Ed.* **2008**, *47*, 2930.

[21] D. McNulty, D. N. Buckley, C. O'Dwyer, *J. Solid State Electrochem.* **2016**, *20*, 1445.

[22] M. Osiak, H. Geaney, E. Armstrong, C. O'Dwyer, *J. Mater. Chem. A* **2014**, *2*, 9433.

[23] H. Gao, L. Xiao, I. Plümel, G.-L. Xu, Y. Ren, X. Zuo, Y. Liu, C. Schulz, H. Wiggers, K. Amine, *Nano Lett.* **2017**, *17*, 1512.

[24] W. Liu, S. Ju, X. Yu, *ACS Nano* **2020**, *14*, 974.

[25] Z. Yu, J. Song, D. Wang, D. Wang, *Nano Energy* **2017**, *40*, 550.

[26] Y. Liu, Q. Liu, Q. Jian, D. Cui, M. Chen, Z. Li, T. Li, T. Nilges, K. He, Z. Jia, C. Zhou, *Nat. Commun.* **2020**, *11*, 2520.

[27] R. Tian, A. Griffin, M. McCrystall, M. Breshears, A. Harvey, C. Gabbett, D. V. Horváth, C. Backes, Y. Jing, T. Heine, S. H. Park, J. Coelho, V. Nicolosi, M. Nentwig, C. Benndorf, O. Oeckler, J. N. Coleman, *Adv. Energy Mater.* **2021**, *11*, 2002364.

[28] Y. Liu, X. He, D. Hanlon, A. Harvey, J. N. Coleman, Y. Li, *ACS Nano* **2016**, *10*, 8821.

[29] C. J. Zhang, M. Liang, S.-H. Park, Z. Lin, A. Seral-Ascaso, L. Wang, A. Pakdel, C. O. Coileain, J. Boland, O. Ronan, *Energy Environ. Sci.* **2020**, *13*, 2124.

[30] Y. An, Y. Tian, Y. Zhang, C. Wei, L. Tan, C. Zhang, N. Cui, S. Xiong, J. Feng, Y. Qian, *ACS Nano* **2020**, *14*, 17574.

[31] R. Tian, N. Alcala, S. J. K. O'Neill, D. V. Horvath, J. Coelho, A. J. Griffin, Y. Zhang, V. Nicolosi, C. O'Dwyer, J. N. Coleman, *ACS Appl. Energy Mater.* **2020**, *3*, 2966.

[32] C. Gabbett, C. S. Boland, A. Harvey, V. Vega-Mayoral, R. J. Young, J. N. Coleman, *Chem. Mater.* **2018**, *30*, 5245.

[33] S. H. Park, P. J. King, R. Y. Tian, C. S. Boland, J. Coelho, C. F. Zhang, P. McBean, N. McEvoy, M. P. Kremer, D. Daly, J. N. Coleman, V. Nicolosi, *Nat. Energy* **2019**, *4*, 560.

[34] J. N. Coleman, *Adv. Funct. Mater.* **2009**, *19*, 3680.

[35] J. N. Coleman, M. Lotya, A. O'Neill, S. D. Bergin, P. J. King, U. Khan, K. Young, A. Gaucher, S. De, R. J. Smith, *Science* **2011**, *331*, 568.

[36] V. Nicolosi, M. Chhowalla, M. G. Kanatzidis, M. S. Strano, J. N. Coleman, *Science* **2013**, *340*, 1226419.

[37] Z. Li, R. J. Young, C. Backes, W. Zhao, X. Zhang, A. A. Zhukov, E. Tillotson, A. P. Conlan, F. Ding, S. J. Haigh, K. S. Novoselov, J. N. Coleman, *ACS Nano* **2020**, *14*, 10976.

[38] C. Backes, D. Campi, B. M. Szydlowska, K. Synnatschke, E. Ojala, F. Rashvand, A. Harvey, A. Griffin, Z. Sofer, N. Marzari, *ACS Nano* **2019**, *13*, 7050.

[39] A. P. Balan, S. Radhakrishnan, C. F. Woellner, S. K. Sinha, L. Deng, C. de Los Reyes, B. M. Rao, M. Paulose, R. Neupane, A. Apte, *Nat. Nanotechnol.* **2018**, *13*, 602.

[40] H. Kaur, R. Tian, A. Roy, M. McCrystall, D. V. Horvath, G. L. Onrubia, R. Smith, M. Ruether, A. Griffin, C. Backes, *ACS Nano* **2020**, *14*, 13418.

[41] T. Chen, H. Kaur, M. McCrystall, R. Tian, A. Roy, R. Smith, D. V. Horvath, J. Maughan, B. Konkena, M. Venkatesan, *FlatChem* **2022**, *33*, 100360.

[42] C. Gibaja, D. Rodríguez-San-Miguel, W. S. Paz, I. Torres, E. Salagre, P. Segovia, E. G. Michel, M. Assebban, P. Ares, D. Hernández-Maldonado, *Adv. Mater.* **2021**, *33*, 2006826.

[43] Y. Wang, R. Cai, J. Zhang, J. Cui, Y. Qin, Y. Zhang, J. Wu, K. Chatterjee, P. M. Ajayan, Y. Wu, *J. Phys. Chem. Lett.* **2020**, *11*, 8668.

[44] H. Kaur, R. Tian, A. Roy, M. McCrystall, R. Smith, D. V. Horvath, V. Nicolosi, J. N. Coleman, *FlatChem* **2021**, *30*, 100295.

[45] Y. Guo, A. Gupta, M. S. Gilliam, A. Debnath, A. Yousaf, S. Saha, M. D. Levin, A. A. Green, A. K. Singh, Q. H. Wang, *Nanoscale* **2021**, *13*, 1652.

[46] H. Kaur, J. N. Coleman, *Adv. Mater.* **2022**, *34*, 2202164.

[47] G. Guan, J. Xia, S. Liu, Y. Cheng, S. Bai, S. Y. Tee, Y. W. Zhang, M. Y. Han, *Adv. Mater.* **2017**, *29*, 1700326.

[48] Z. Tai, C. M. Subramaniyam, S. L. Chou, L. Chen, H. K. Liu, S. X. Dou, *Adv. Mater.* **2017**, *29*, 1700605.

[49] A. P. Balan, S. Radhakrishnan, R. Kumar, R. Neupane, S. K. Sinha, L. Deng, C. A. de los Reyes, A. Apte, B. M. Rao, M. Paulose, *Chem. Mater.* **2018**, *30*, 5923.

[50] Q. Fan, C. Choi, C. Yan, Y. Liu, J. Qiu, S. Hong, Y. Jung, Z. Sun, *Chem. Commun.* **2019**, *55*, 4246.

[51] H. Li, L. Jing, W. Liu, J. Lin, R. Y. Tay, S. H. Tsang, E. H. T. Teo, *ACS Nano* **2018**, *12*, 1262.

[52] S. Zhang, H. j. Qian, Z. Liu, H. Ju, Z. y. Lu, H. Zhang, L. Chi, S. Cui, *Angew. Chem.* **2019**, *131*, 1673.

[53] K. R. Paton, E. Varrla, C. Backes, R. J. Smith, U. Khan, A. O'Neill, C. Boland, M. Lotya, O. M. Istrate, P. King, *Nat. Mater.* **2014**, *13*, 624.

[54] U. Khan, A. O'Neill, M. Lotya, S. De, J. N. Coleman, *Small* **2010**, *6*, 864.

[55] J. Texter, *Angew. Chem., Int. Ed. Engl.* **2015**, *54*, 10258.

[56] P. G. Karagiannidis, S. A. Hodge, L. Lombardi, F. Tomarchio, N. Decorde, S. Milana, I. Goykhman, Y. Su, S. V. Mesite, D. N. Johnstone, *ACS Nano* **2017**, *11*, 2742.

[57] Y. Zhu, J. Ren, X. Zhang, D. Yang, *Nanoscale* **2020**, *12*, 13297.

[58] C.-M. Fung, C.-C. Er, L.-L. Tan, A. R. Mohamed, S.-P. Chai, *Chem Rev* **2021**, *122*, 3879.

[59] C. Backes, R. J. Smith, N. McEvoy, N. C. Berner, D. McCloskey, H. C. Nerl, A. O'Neill, P. J. King, T. Higgins, D. Hanlon, *Nat. Commun.* **2014**, *5*, 4576.

[60] A. Harvey, C. Backes, J. B. Boland, X. He, A. Griffin, B. Szydlowska, C. Gabbett, J. F. Donegan, J. N. Coleman, *Nat. Commun.* **2018**, *9*, 4553.

[61] Y. Xuan, H. Quan, Z. Shen, C. Zhang, X. Yang, L. L. Lou, S. Liu, K. Yu, *Chemistry* **2020**, *26*, 2285.

[62] E. N. Rissi, E. Soignard, K. A. McKiernan, C. J. Benmore, J. L. Yarger, *Solid State Commun.* **2012**, *152*, 390.

**ADVANCED
SCIENCE NEWS**

www.advancedsciencenews.com

**ADVANCED
ENERGY
MATERIALS**

www.advenergymat.de

[63] J. M. Zaug, A. K. Soper, S. M. Clark, *Nat. Mater.* **2008**, *7*, 890.

[64] X. Wu, K. Gong, G. Zhao, W. Lou, X. Wang, W. Liu, *RSC Adv.* **2018**, *8*, 4595.

[65] C. Backes, B. M. Szydłowska, A. Harvey, S. Yuan, V. Vega-Mayoral, B. R. Davies, P.-l. Zhao, D. Hanlon, E. J. G. Santos, M. I. Katsnelson, *ACS Nano* **2016**, *10*, 1589.

[66] D. Hanlon, C. Backes, E. Doherty, C. S. Cucinotta, N. C. Berner, C. Boland, K. Lee, A. Harvey, P. Lynch, Z. Gholamvand, *Nat. Commun.* **2015**, *6*, 8563.

[67] N. Sleiman, V. Deluchat, M. Wazne, A. Courtin, Z. Saad, V. Kazpard, M. Baudu, *RSC Adv.* **2016**, *6*, 1627.

[68] H. Kaur, R. Tian, A. Roy, M. McCrystall, D. V. Horvath, G. L. Onrubia, R. Smith, M. Ruether, A. Griffin, C. Backes, *ACS Nano* **2021**, *15*, 9196.

[69] V. Vega-Mayoral, R. Y. Tian, A. G. Kelly, A. Griffin, A. Harvey, M. Borrelli, K. Nisi, C. Backes, J. N. Coleman, *Nanoscale* **2019**, *11*, 6206.

[70] Y. Liu, X. He, D. Hanlon, A. Harvey, U. Khan, Y. Li, J. N. Coleman, *ACS Nano* **2016**, *10*, 5980.

[71] J. B. Boland, R. Tian, A. Harvey, V. Vega-Mayoral, A. Griffin, D. V. Horvath, C. Gabbett, M. Breshears, J. Pepper, Y. Li, J. N. Coleman, *2D Mater.* **2020**, *7*, 035015.

[72] H. Sun, D. Hanlon, D. A. Dinh, J. B. Boland, A. E. D. R. Castillo, C. Di Giovanni, A. Ansaldo, V. Pellegrini, J. N. Coleman, F. Bonaccorso, *2D Mater.* **2017**, *5*, 015024.

[73] J. B. Boland, A. Harvey, R. Tian, D. Hanlon, V. Vega-Mayoral, B. Szydlowska, A. Griffin, T. Stimpel-Lindner, S. Jaskaniec, V. Nicolosi, *Nanoscale Adv.* **2019**, *1*, 1560.

[74] T.-H. Hsu, W.-R. Liu, *Polymers* **2020**, *12*, 1162.

[75] S. Liu, J. Feng, X. Bian, J. Liu, H. Xu, Y. An, *Energy Environ. Sci.* **2017**, *10*, 1222.

[76] X. Ma, L. Chen, X. Ren, G. Hou, L. Chen, L. Zhang, B. Liu, Q. Ai, L. Zhang, P. Si, J. Lou, J. Feng, L. Ci, *J. Mater. Chem. A* **2018**, *6*, 1574.

[77] Z. Yu, J. Song, D. Wang, D. Wang, *Nano Energy* **2017**, *40*, 550.

[78] Y. Zhu, Y. Wen, X. Fan, T. Gao, F. Han, C. Luo, S.-C. Liou, C. Wang, *ACS Nano* **2015**, *9*, 3254.

[79] Y. Kim, Y. Park, A. Choi, N. S. Choi, J. Kim, J. Lee, J. H. Ryu, S. M. Oh, K. T. Lee, *Adv. Mater.* **2013**, *25*, 3045.

[80] J. M. Sangster, *J. Phase Equilib. Diffus.* **2010**, *31*, 62.

[81] Y. Liu, N. Zhang, X. Liu, C. Chen, L.-Z. Fan, L. Jiao, *Energy Storage Mater.* **2017**, *9*, 170.

[82] L. Li, Y. Zheng, S. Zhang, J. Yang, Z. Shao, Z. Guo, *Energy Environ. Sci.* **2018**, *11*, 2310.

[83] W. Liu, L. Du, S. Ju, X. Cheng, Q. Wu, Z. Hu, X. Yu, *ACS Nano* **2021**, *15*, 5679.

[84] Y. Chai, X. Wang, Y. Yu, X. Shi, Q. Zhang, N. Wang, *Int. J. Energy Res.* **2019**, *43*, 6045.

[85] S. Fleischmann, J. B. Mitchell, R. Wang, C. Zhan, D. E. Jiang, V. Presser, V. Augustyn, *Chem. Rev.* **2020**, *120*, 6738.

[86] D. V. Horvath, J. Coelho, R. Tian, V. Nicolosi, J. N. Coleman, *ACS Appl. Energy Mater.* **2020**, *3*, 10154.

[87] D. V. Horvath, R. Tian, C. Gabbett, V. Nicolosi, J. N. Coleman, *J. Electrochem. Soc.* **2022**, *169*, 030503.

[88] S.-H. Park, R. Tian, J. Coelho, V. Nicolosi, J. N. Coleman, *Adv. Energy Mater.* **2019**, *9*, 1901359.

[89] R. Tian, S.-H. Park, P. J. King, G. Cunningham, J. Coelho, V. Nicolosi, J. N. Coleman, *Nat. Commun.* **2019**, *10*, 1933.

[90] R. Tian, M. Breshears, D. V. Horvath, J. N. Coleman, *ACS Nano* **2020**, *14*, 3129.

[91] W. Li, S. Hu, X. Luo, Z. Li, X. Sun, M. Li, F. Liu, Y. Yu, *Adv. Mater.* **2017**, *29*, 1605820.

[92] S. H. Park, R. Y. Tian, J. Coelho, V. Nicolosi, J. N. Coleman, *Adv. Energy Mater.* **2019**, *9*, 1901359.

[93] J. Wu, Z. Ju, X. Zhang, C. Quilty, K. J. Takeuchi, D. C. Bock, A. C. Marschilok, E. S. Takeuchi, G. Yu, *ACS Nano* **2021**, *15*, 19109.

[94] Y. D. Kuang, C. J. Chen, G. Pastel, Y. J. Li, J. W. Song, R. Y. Mi, W. Q. Kong, B. Y. Liu, Y. Q. Jiang, Y. Yang, L. B. Hu, *Adv. Energy Mater.* **2018**, *8*, 1802398.

[95] H. T. Sun, L. Mei, J. F. Liang, Z. P. Zhao, C. Lee, H. L. Fei, M. N. Ding, J. Lau, M. F. Li, C. Wang, X. Xu, G. L. Hao, B. Papandrea, I. Shakir, B. Dunn, Y. Huang, X. F. Duan, *Science* **2017**, *356*, 599.